Geir Kulia

Investigation of distortions in microgrids

Master's thesis
for the degree of Master of Science

Trondheim, October 2016

Supervised by Lars Lundheim and Marta Molinas

Norwegian University of Science and Technology
The Faculty of Information Technology, Mathematics and Electrical Engineering
Department of Electronics and Telecommunications

NTNU
Norwegian University of
Science and Technology

NTNU

Norwegian University of Science and Technology

Master's thesis
for the degree of Master of Science

The Faculty of Information Technology, Mathematics and Electrical Engineering
Department of Electronics and Telecommunications

Master thesis at NTNU,

Printed by NTNU-trykk

Abstract

English

This thesis presents a validation study based on data analysis aimed at identifying the cause of atypical behavior observed in a microgrid's data. The data of a stand-alone PV microgrid in Bhutan is analyzed. The analysis of the voltage waveform distortions found in the data is utilizing the Hilbert-Huang Transform (HHT) and periodograms. The Hilbert-Huang Transform shows an oscillating frequency with fluctuations of 10 ms, while the fundamental frequency component's period is 20 ms. As we couldn't attribute this distortion to a nonlinear load, we first argue that the most probable cause of the distortion is a 100 Hz oscillation commonly known to exist on the dc bus.

The Periodogram shows a dominance of odd harmonics, with particular emphasis on 50 and 150 Hz. The analysis reveals that the dominance of the third harmonic can be explained by multiplication in the microgrid's controller. There are two interpretations for the other odd harmonics. The pulse-width modulation and unideal low pass filtering cause odd harmonics on the ac side of the inverter. The same does a harmonic feedback from the ac bus to the dc via the inverter. The harmonic feedback creates a positive feedback loop through the controller resulting in odd harmonics on the ac side and even harmonics on the dc side.

The thesis will also compare the voltage data measured on a physical grid with a mathematical model of the system and a simulation to test the hypothesis of the distortion's origin. This test goes far in confirming the hypothesis of the source of the distortions.

Samandrag

Nynorsk

Denne avhandlinga presenterer eit validitetsstudium der bølgjeformer frå elektriske spenningar blir analyserte for å identifisere atypiske forvrengingar i spenningsforsyninga i eit mikroenergiverk. Dataa som er brukte i analysen kjem frå eit frittståande solcellebasert mikroenergiverk i Bhutan. Dei elektriske bølgjeformene blir analyserte ved hjelp av Hilbert Huang-transformasjonen (HHT) og periodogramm. Hilbert Huang-transformasjonen viste ein varierande frekvens med svingingar som hadde 10 ms-periodar på monokomponenten til grunnfrekvensen, som også hadde ein grunnperiode på 20 ms. Den mest sannsynlege forklaringa for dette fenomenet er ein 100 Hz svinging som ofte er observert på dc-sida av slike energiverk. Grunnfrekvensen hadde også aperiodiske svingingar, men dei blei ikkje vidare studert i denne avhandlinga. Periodogrammet var dominert av oddetalharmoniske, der 50 Hz og 150 Hz hadde høgast effekt. Ein systemanalyse viste at den høge effekten rundt 150 Hz er eit resultat av ein multiplikasjon av to sinusforma bølgjer i mikroenergiverket si kontrolleining. Det er to forklaringar på dei andre oddetalharmoniske. Pulsviddemodulasjon og ikkje-ideel lågpassfiltrering genererer oddetalharmoniske på ac-sida av mikrokraftverket. Det gjer også ei harmonisk tilbakekopling frå ac-sida til dc-sida av invertaren. Avhandlinga vil også samanlikne spenningsmålingane med ein matematisk modell av systemet og ei simulering for å teste hypotesane om årsakene til forvrengingane. Testane stadfestar i stor grad at forvrengingane på ac-sida kan sporast tilbake dc-sida.

Sammendrag

Bokmål

Denne avhandlingen presenterer et validitetsstudie der bølgeformer fra elektriske spenninger blir analysert for å identifisere atypiske forvrengninger i spenningsforsyningen i et mikroenergiverk. Dataene som er brukt i analysen kommer fra et frittstående solcellebasert mikroenergiverk i Bhutan. De elektriske bølgeformene analyseres ved hjelp av Hilbert-Huang transformasjon (HHT) og Periodogramm. Hilbert-Huang transformasjonen viste en varierende frekvens med svingninger som hadde 10 ms perioder på grunnfrekvensen sin monokomponent, som også hadde grunnperiode på 20 ms. Den mest sannsynlige forklaringen for dette fenomenet er en 100 Hz svingning som ofte er observert på dc-siden av slike energiverk. Grunnfrekvensen hadde også aperiodiske svingninger, men de ble ikke videre studert i denne avhandlingen. Periodogrammet var dominert av oddetalls harmoniske, der 50 Hz og 150 Hz hadde høyest effekt. En systemanalyse viste at den høye effekten rundt 150 Hz er et resultat av en multiplikasjon av to sinusformede bølger i mikroenergiverkets kontrollenhet. Det er to forklaringer på de andre odde harmoniske. Pulsviddemodulasjon og ikke ideell lavpass filtrering generer odde harmoniske på ac-siden av mikrokraftverket. Det gjør også en harmonisk tilbakekobling fra ac-siden til dc-siden av inverteren. Den harmoniske tilbakekoblingen lager en tilbakekoblingssløyfe via kontrolleren. Dette resulterer i odde harmoniske på ac-siden og likeharmoniske på dc-siden av inverteren. Avhandlingen vil også sammenligne spenningsmålingene med en matematisk modell av systemet og en simulering for å teste hypotesene om forvrengingene sine årsaker. Testene bekrefter i stor grad at forvrengingene på ac-siden kan spores tilbake til dc-siden.

Acknowledgments

First, I would like to thank *Marta Molinas* for the creative ideas behind this project, organizing the field trip to Bhutan, and for being a mentor, conversation partner, and friend throughout this project. Her creative ideas and critical thinking never cease to amaze me.

Secondly, I want to thank my supervisor *Lars Lundheim* for his patience, creativity, and academic integrity. Your explanations are always intuitive, and your eye for details has been in high demand during this project.

Olav Fosso has been providing advice, validation, and encouragement during this project. It is much appreciated.

I am grateful to *Bjørn B. Larsen* for formally facilitating the initialization of this project, and his supervision.

Special thanks are in order to *Norden Huang* for personally giving insight into his methods, both in Taiwan and in Norway. His open-mindedness and generosity has been highly appreciated.

Mohammad Amin and *Paula B. Garcia Rosa* has been excellent interlocutors when discussing problems and solutions in both power electronics and signal analysis. Thank you.

I would like to acknowledge the contribution of *Jon Are Suul* for providing help with simulation setup of a single phase inverter during a stressful period.

The data analysis would not have been verified without the measurements at RUB. It is therefore in place to thank *Tshewang Lhendupand*, *Cheku Dorji*, my travel partner and coworker *Håkon Duus* and all the staff and students at CST that we cooperated with for their assistance in collecting data from the microgrids. My

time at CST has been a truly unique experience. The field trip to Bhutan was partially supported by Ren-Peace, IUG NTNU, and Department of Electronics and Telecommunications at NTNU. Thank you.

Thanks are in order to *Knut Andreas Eikland Bækkelie* and *Kristoffer Venæs Monsen* for correcting the language of this thesis. It has been much needed. I would also like to thank *Elise Tørring* for helping me with the Nynorsk Norwegian version of the abstract.

Last, but far from least, thank you *Brenda Huang*, for your love when I am stressed, for motivation when I'm unproductive, and for always continuously supporting me during the writing of this thesis.

(Freepik designed most icons in this thesis.)

Contents

List of Tables xiii

List of Figures xvii

List of Acronyms xix

List of Symbols xxi

1 Motivation 1

2 Description of the microgrid system 3

3 Analysis of electrical signals from the microgrid 7

3.1 Power spectrum 7

3.2 Hilbert-Huang transform 8

3.2.1 Hilbert transform and the Bedrosian theorem 9

3.2.2 Normalized Quadrature method 11

3.2.3 Instantaneous frequency 13

3.2.4 Demonstration of the Hilbert-Huang transform 14

3.2.5 Hilbert-Huang transform of measured voltage waveform . 14

3.3 Suggested hypothesis for the root of distortions 17

4 Modeling and analytical investigation of the hypothesis 21

4.1 Analytical investigation of the hypothesis 24

4.1.1 Power spectrum and pulse-width modulation 24

4.1.2 Hilbert spectrum 27

5 Validation of the hypothesis with simulation 31

5.1 Power spectrum 32

5.2 Hilbert spectrum 32

6 Positive feedback cascading effect as cause of distortion 37

6.1 Discussion 40

7 Reflections on the hypothesis 41

8 Concluding remarks 45

A Example of the Hilbert transform and Normalized Quadrature Method 51

A.1 Hilbert transform 51

A.2 Normalized Quadrature method 52

B Calculation of $v_{\text{control}}(t)$ 55

C The ac voltage's effect on the dc bus through the inverter 59

D Square of sum containing odd harmonics 61

E Comments on amplitude variations 63

List of Tables

4.1 Microgrid model parameters. 25

List of Figures

2.1 Schematics of the microgrid at RUB College of Science and Technology. 3

2.2 The measured $v_{\mathrm{ac,m}}(t)$ compared with a pure sinusoid. 4

3.1 Power spectrum of $v_{\mathrm{ac,m}}(t)$. The spectrum is calculated using (3.1) where $N = 178$ and $F_s = 8.9$ KHz. 8

3.2 UML activity diagram of the Empirical Mode Decomposition (EMD) algorithm 10

3.3 Example for figures for the Normalized Quadrature method. . . . 12

3.4 Example of a signal and its decomposition using Empirical Mode Decomposition. 15

3.5 Hilbert spectrum of $v(t)$. 15

3.6 Hilbert-Huang transform of $v_{\mathrm{ac,m}}(t)$. 16

3.7 Problem with Euler forward derivation example 16

3.8 Hilbert spectrum of $v_{\mathrm{ac,mg}}(t)$. 17

3.9 Thévenin equivalent of dc power supply. 19

4.1 High level model of the microgrid investigated in this thesis. . . . 22

4.2 $v_{\mathrm{ac,a}}(t)$ from (4.11) against an ideal ac voltage waveform as in (2.1). 24

4.3 Power spectrum of $v_{\mathrm{ac,a}}(t)$. 25

4.4 Numerical estimation of the pwm effect on $v_{\mathrm{ac,a}}(t)$. 26

4.5 Pulse-width modulated voltage $v_{\mathrm{pwm}}(t)$ generated by comparing a generated triangular signal $v_{\mathrm{tri}}(t)$ with $v_{\mathrm{control}}(t)$. 26

4.6 Power spectrum of $v_{\mathrm{ac,n}}(t)$. The spectrum is calculated using (3.1) where $N = 2000$ and $F_s = 100$ KHz. 27

4.7 Hilbert spectrum of $v_{\mathrm{ac,a}}(t)$. 27

4.8 The intrinsic mode functions describing $v_{\mathrm{ac,n}}(t)$. 28

4.9 Hilbert spectra of $v_{\mathrm{ac,n}}(t)$. 29

5.1 Simulated $v_{\mathrm{ac,s}}(t)$ and $v_{d,s}(t)$. 31

5.2 Power spectrum of $v_{\mathrm{ac,s}}(t)$. The spectrum is calculated using (3.1) where $N = 20$ K and $F_s = 1$ MHz. 32

5.3 The simulated $v_{\mathrm{ac,s}}$'s intrinsic mode functions. 33

5.4 Hilbert spectrum of $v_{\mathrm{ac,s}}(t)$. 33

5.5 Hilbert spectrum of $v_{\mathrm{ac,s}}(t)$. 34

5.6 Simulink schematics of the main blocks of the microgrid simulation. 35

6.1 High level model of the microgrid investigated in this thesis. . . . 37

6.2 Abstraction of the microgrid model. 38

6.3 Power spectrum of simulated dc bus $v_{d,\mathrm{s}}(t)$ and ac voltage $v_{\mathrm{ac,s}}(t)$. The spectrum is calculated using (3.1) where $N = 20$ K and $F_s = 1$ MHz. 40

7.1 The instantaneous frequency from the grid component of the measured waveform $f_{\mathrm{ac,mg}}(t)$, result of the analytic investigation $f_{\mathrm{ac,ag}}(t)$ and its numeric version corrected for pwm $f_{\mathrm{ac,ng}}(t)$, and from the simulation $f_{\mathrm{ac,sg}}(t)$ shown together. 41

7.2 The power spectra from the grid component of the measured waveform $P_{\mathrm{ac,m}}(\omega)$, result of the analytic investigation $P_{\mathrm{ac,a}}(\omega)$ and its numeric version corrected for pwm $P_{\mathrm{ac,n}}(t)$, and from the simulation $P_{\mathrm{ac,s}}(\omega)$ shown together. 42

A.1 Voltage waveform $v_1(t)$ and its instantaneous frequency $f_1(t)$ calculated using discrete Hilbert transform. The Bedrosian theorem is satisfied for $v_1(t)$. 52

A.2 Power spectra of $V_2(t)$ and $\cos\big(\theta_2(t)\big)$. 52

A.3 Voltage waveform $v_2(t)$ and its instantaneous frequency $f_2(t)$ calculated using the discrete Hilbert transform and normalized quadrature method. 53

E.1 The instantaneous amplitudes from the grid component of the measured waveform $V_{\mathrm{ac,mg}}(t)$, result of the analytic investigation $V_{\mathrm{ac,ag}}(t)$, and from the simulation $V_{\mathrm{ac,sg}}(t)$ shown together. 63

List of Acronyms

NTNU Norwegian University of Science and Technology

RUB Royal University of Bhutan

CST College of Science and Technology

PV photovoltaic

HHT Hilbert-Huang Transform

EMD Empirical Mode Decomposition

IMF Intrinsic mode function

dc direct current

ac alternating current

pwm pulse-width modulation

pu per-unit

PI controller proportional integral controller

RC proportional resonant controller

LP low pass

UML Unified Modeling Language

FE Forward Euler

NQM Normalized quadrature method

PCHIP Piecewise Cubic Hermite Interpolating Polynomial

rad radian

List of Symbols

Constants

π the ratio of a circle's circumference to its diameter

e base of natural logarithm

j imaginary unit which satisfies $j^2 = -1$

General consepts

N_{imf} total number of IMFs

N total number of samples

T_s Sampling period

F_s Sampling frequency

n discrite time variable, counting variable, or odd numbers

t continuous time variable

τ continuous time variable

Δt time difference

$P(\omega)$ power spectrum of $v(t)$

$P_{\mathrm{ac}}(\omega)$ power spectrum of $v_{\mathrm{ac}}(t)$

$P_{\mathrm{ac,m}}(\omega)$ power spectrum of $v_{\mathrm{ac,m}}(t)$

$P_{\mathrm{ac,a}}(\omega)$ power spectrum of $v_{\mathrm{ac,a}}(t)$

$P_{\mathrm{ac,n}}(\omega)$ power spectrum of $v_{\mathrm{ac,n}}(t)$

$P_{\mathrm{ac,s}}(\omega)$ power spectrum of $v_{\mathrm{ac,s}}(t)$

$v(t)$ arbitrary example voltage

$v_i(t)$ arbitrary example voltage IMF

$V_i(t)$ v_i's instantaneous amplitude

$\hat{v}_i(t)$ $v_i(t)$ normalized between -1 and 1 ($\frac{v_i(t)}{V_i(t)}$)

$v_r(t)$ residue voltage after EMD

$\theta_i(t)$ v_i's phase

$\omega_i(t)$ v_i's instantaneous angle frequency

$f_i(t)$ v_i's instantaneous frequency

$\mathscr{H}\big(v(t)\big)$ Hilbert transform of $v(t)$

$H_i(\omega, t)$ Hilbert spectrum of one IMF

$H(\omega, t)$ Hilbert spectrum of all IMFs in a given multicomponent

$v_{\mathrm{pu}}(t)$ arbitrary voltage in per unit

$v_{\mathrm{volt}}(t)$ arbitrary voltage in volt

$V_{\mathrm{base}}(t)$ arbitrary base voltage amplitude in volt

k determine if quadrature is positive or negative

$z(t)$ v's analytic signal

$\delta(\omega)$ Dirac delta function

a constant amplitude used for mathematical demonstration

b constant amplitude used for mathematical demonstration

G constant amplitude used for mathematical demonstration

ϕ_G phase shift used for mathematical demonstration

i counting variable

k counting variable

Microgrid model

$P_{\mathrm{ac}}(t)$ ac power consumed by the load

$v_{\mathrm{ac}}(t)$ ac voltage waveform delivered to the load

V_{ac} optimal grid amplitude voltage ($230\sqrt{2}$ Volt)

$i_{\mathrm{ac}}(t)$ ac current waveform delivered to the load

I_{ac} amplitude of ac current $i_{\mathrm{ac}}(t)$

ϕ_i the phase shift between $i_{\mathrm{ac}}(t)$ and $v_{\mathrm{ac}}(t)$

$P_d(t)$ dc power provided by the PV power source

$v_d(t)$ dc voltage

$v_{d,\mathrm{s}}(t)$ simulated dc voltage

$V_d(t)$ constant part of dc voltage

$\tilde{v}_d(t)$ time-varying part of $v_d(t)$

$\tilde{V}_d(t)$ $\tilde{v}_d$'s amplitude

$i_d(t)$ dc current

$I_d(t)$ constant part of dc current

$\tilde{i}_d(t)$ time-varying part of $i_d(t)$

$\tilde{I}_d(t)$ $\tilde{i}_d$'s amplitude

ω_o grid angle frequency ($2\pi 50$ Hz)

f_0 grid frequency (50 Hz)

$v_{\mathrm{ac,m}}(t)$ ac voltage waveform $v_{\mathrm{ac}}(t)$ measured on a physical microgrid system

$v_{\mathrm{ac,a}}(t)$ ac voltage waveform $v_{\mathrm{ac}}(t)$ analytically estimated using a mathematical model

$v_{\mathrm{ac,n}}(t)$ ac voltage waveform $v_{\mathrm{ac,a}}(t)$ numerically corrected for pulse-widt modulation and filters

$v_{\mathrm{ac,s}}(t)$ ac voltage waveform $v_{\mathrm{ac}}(t)$ analytically estimated using a simulink simulation

$v_{\mathrm{ac,md}}(t)$ $v_{\mathrm{ac,m}}(t)$'s IMF containing high frequency distortions

$v_{\mathrm{ac,nd}}(t)$ $v_{\mathrm{ac,n}}(t)$'s IMF containing high frequency distortions

$v_{\mathrm{ac,sd}}(t)$ $v_{\mathrm{ac,s}}(t)$'s IMF containing high frequency distortions

$v_{\mathrm{ac,mg}}(t)$ $v_{\mathrm{ac,m}}(t)$'s IMF corresponding to its grid frequency component

$v_{\mathrm{ac,ag}}(t)$ same as $v_{\mathrm{ac,a}}(t)$. ($v_{\mathrm{ac,ag}}(t) = v_{\mathrm{ac,a}}(t)$)

$v_{\mathrm{ac,ng}}(t)$ $v_{\mathrm{ac,n}}(t)$'s IMF corresponding to its grid frequency component

$v_{\mathrm{ac,sg}}(t)$ $v_{\mathrm{ac,s}}(t)$'s IMF corresponding to its grid frequency component

$v_{\mathrm{control}}(t)$ Control signal from the controller to the inverter and is ideally proportional to the ac voltage $v_{\mathrm{ac}}(t)$

$v_{\mathrm{pwm}}(t)$ pulse-width modulated voltage waveform

$v_{\mathrm{tri}}(t)$ triangle signal used to generate the pulse-width modulated voltage waveform $v_{\mathrm{pwm}}(t)$

V_s Supply voltage (400 V)

R_s Line impedance

R_{load} Load impedance

R_k constant to scale $i_{\mathrm{ac}}(t)$ in the controller

$v_{\mathrm{rc,in}}(t)$ input signal to the RC controller.

$v_{\mathrm{pi}}(t)$ output signal from the PI controller

V_r offset for error signal into the PI controller

$v_e(t)$ Difference between V_r and $v_d(t)$

A Amplitude determined by the PI controller

B Constant to scale $v_{\mathrm{ac}}(t)$ in the controller

B' Constant to scale $v_{\mathrm{ac}}(t)$ in the controller

C_1 Constant determined by the controller

C_2 Constant determined by the controller

C_1' Constant determined by the controller

C_2' Constant determined by the controller

ϕ_1 phase shift determined by the controller

ϕ_2 phase shift determined by the controller

ϕ_{ac} phase shift determined by the controller

ϕ_1' phase shift determined by the controller

ϕ_2' phase shift determined by the controller

ϕ phase shift determined by the PI controller

K_p PI controller's proportional coefficient

K_i PI controller's integral coefficient

C_p RC controller's proportional coefficient

C_i RC controller's resonant coefficient

$H_{\mathrm{lp}}(s)$ transfer function of a low pass filter

$h_{\mathrm{lp}}(t)$ impulse response of a low pass filter

D Constant determined by the controller's tuning

V_{g1} Constant determined by the controller's tuning

V_{g2} Constant determined by the controller's tuning

V_g Constant determined by the controller's tuning

V_{am1} Constant determined by the controller's tuning

V_{am2} Constant determined by the controller's tuning

V_{am} Constant determined by the controller's tuning

ϕ_g phase shift determined by the controller's tuning

ϕ_{am} phase shift determined by the controller's tuning

$v_{\mathrm{ac,rc}}(t)$ the result of $i_{\mathrm{ac}}(t)$ on $v_{\mathrm{control}}(t)$ through the RC controller

$v_{\mathrm{feedback}}(t)$ the result of $i_{\mathrm{ac}}(t)$ on $v_{\mathrm{ac}}(t)$ through the controller

V_a indicate the proportionality factor between $v_d(t)$ and $v_{\mathrm{ac}}^2(t)$.

Chapter 1

Motivation

Universal access to affordable modern power services is one of the United Nations sustainable development goals [1]. Electrical power is the foundation of modern business, medicine, education, agriculture, infrastructure, and communications. Lack of access to electricity is, therefore, a severe impediment to economic growth, yet, this is the case for 1.2 billion people worldwide. Of these 1.2 billion without electricity access, 80 % live in rural areas; 95 % in sub-Saharan Africa or in developing Asia [2]. Applying islanded, i.e. not grid connected, microgrids with free renewable energy sources is an alternative for providing electricity to isolated communities where extending the main grid is too expensive. Microgrids are electrical systems that locally generate, store and provide power to a small area, such as a village. Traditionally, these grids have often been utilizing diesel aggregates, but due to the recent fall in prices for photovoltaic (PV) cells, PV based microgrids have become a conspicuous substitute that can provide cleaner and cheaper electricity.

Because of the nature of the location for where the islanded microgrids are desirable, the microgrids needs to be near maintenance free and have a supervisory control system that can handle any faults that might occur. Due to the stochastic nature of PV sources and the nonlinearities of modern power electronic equipment that are essential microgrid components, the need for accurate monitoring and diagnosis devices based on measurement of instantaneous values of fundamental electrical parameters rather than average values has become apparent. This initiative is part of a greater partnership with the Royal University of Bhutan (RUB)'s College of Science and Technology (CST) which aim at developing reliable and affordable solutions for easy diagnosis and correction of potential problems of microgrids in rural areas. The partnership has been the foundation for several master's theses

and projects at NTNU [3, 4, 5]. The distortions on the ac bus are traditionally associated with nonlinear loads. In a previous contribution, the author of this thesis presented, together with supervisors, a method for decomposing and analyzing electrical voltage and current waveforms to estimate the instantaneous frequency [6] by applying the Hilbert-Huang Transform [7]. We then suggested that the electrical waveforms were a fluctuating frequency with 10 ms repetitions, and made a hypothesis that this might be the result of the controller, and not the load.

This thesis is based on and will elaborate a validation study where we tested the hypothesis by investigating the underlying system behind the microgrid [8]. The validation procedure consists of comparing results observed in the field data with an analytical model of the distortion, supported by simulation data from a detailed Matlab model which then are used to discuss the hypothesis. The results from the analytical model and the simulation model exhibit seemingly non-periodic properties of the instantaneous frequencies when compared with the measured waveforms obtained at RUB CST's stand-alone microgrid. The expected grid frequency in such systems should be a stationary 50 Hz, while the observed frequencies in this investigation show a distorted oscillatory frequency with cycles of 10 ms on the grid frequency.

By better understanding the cause of the phenomena behind the distortions on the microgrid, we gain better knowledge on how to design and tune the inverters to easier suit the environment where they will be applied. The author hopes this can help to lay a foundation of a methodology to diagnose microgrids so that we can contribute to providing more reliable and less maintenance demanding electricity access to rural areas in the developing world.

Chapter 2

Description of the microgrid system

Systems to generate electrical energy does traditionally rely on converting mechanical or thermal energy into electrical energy directly, where a large mass with considerable momentum and inertia rotate. This natural inertia helps to maintain a stable frequency. Many of the underlying assumptions of the electrical systems originate in this kind of systems. As modern electrical power production more frequently relies on steady-state power electronics, we cannot expect to have the same innate inertia in the future.

Cooperation between Royal Univeristy of Bhutan's college of science and technology and NTNU led us to conduct experiments on their microgrids where we measured voltage and current waveforms. Their single-bridge (one phase) microgrids

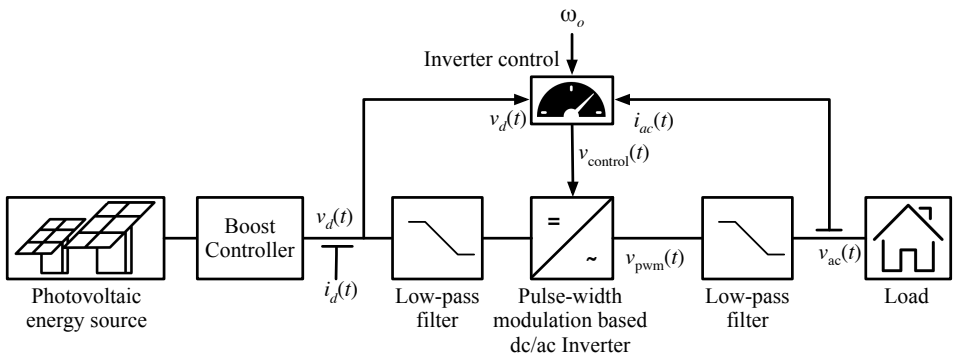

Figure 2.1: Schematics of the microgrid at RUB College of Science and Technology.

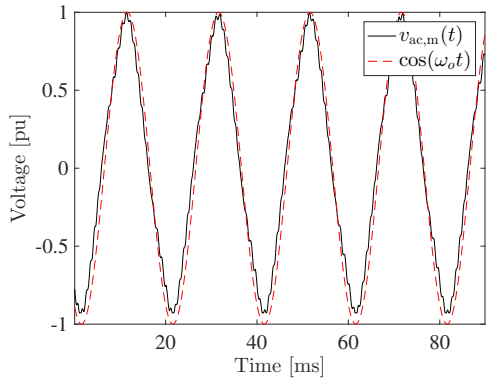

Figure 2.2: The measured $v_{\mathrm{ac,m}}(t)$ compared with a pure sinusoid.

aim to mimic microgrids with the same type of load, climate, and electrical setup as a microgrid in an isolated community. Figure 2.1 depict a model of the microgrid. It has a photovoltaic source. A boost controller is used to maintain a stable dc voltage $v_d(t)$. The dc voltage is converted to ac by a steady-state dc/ac inverter based on pulse-width modulation (pwm). The pwm voltage v_{pwm} is filtered using a low-pass filter to achieve a smooth ac voltage waveform $v_{\mathrm{ac}}(t)$ to the load. The inverter's controller keeps the grid frequency stable on the ac voltage $v_{\mathrm{ac}}(t)$ by using the ac current $i_{\mathrm{ac}}(t)$, the dc voltage $v_{\mathrm{d}}(t)$, and the reference frequency ω_o as a reference. The load is mostly linear, according to the employees at the college. The output voltage should ideally be given by

$$v_{\mathrm{ac}}(t) = V_{\mathrm{ac}} \cdot \cos(\omega_o t). \tag{2.1}$$

V_{ac} is the desired amplitude of $v_{\mathrm{ac}}(t)$ and is $230\sqrt{2}$ Volt in Bhutan. The angle frequency is given by

$$\omega_o = 2\pi f_o \tag{2.2}$$

f_o is the grid-frequency. The grid-frequency in Bhutan is $f_o = 50$ Hz.

We had the opportunity to measure $v_{\mathrm{ac,m}}(t)$ and $i_{\mathrm{ac,m}}(t)$ when performing the experiments. The letter m is added in subscript to indicate that the waveform is measured. The voltage waveform $v_{\mathrm{ac,m}}(t)$ of the stand-alone microgrid is shown in figure 2.2. The red-dotted line shows ideal conditions as given by (2.1). $v_{\mathrm{ac,m}}(t)$ is considerably more distorted compared with the main grid in Bhutan [6]. The unit is in per-unit (pu) instead of Volt [9]. The per-unit system allows expressions with

large absolute values to be expressed as a fraction in the form given by

$$v_{\mathrm{pu}}(t) = \frac{v_{\mathrm{volt}}(t)}{V_{\mathrm{base}}} \tag{2.3}$$

where V_{base} is an arbitrarily chosen base value unit. The motivation for using the per-unit system is to simplify calculations and enable easy comparison between signals with a large difference in absolute value, such as ac voltages on the output of the inverter and internal signals in the controller. The per-unit system is used for power, voltage, current, impedance, and admittance, and is widely used by manufacturers in the power electronic community. Conversion from the per-unit system requires knowledge about the base unit.

The voltage waveform $v_{\mathrm{ac,m}}(t)$ is distorted compared with a perfect sinusoid. It has some harmonic distortions giving it local extrema and a general curving towards the left.

Chapter 3

Analysis of electrical signals from the microgrid

It is useful to have systematic and statistical tools when analyzing distortions. We will, therefore, apply the traditional power spectrum and the more recent Hilbert-Huang transform when analyzing the voltage waveform $v_{\mathrm{ac,m}}(t)$ measured at the stand-alone microgrid as discussed in the previous chapter. The power spectrum is optimized for periodic behavior and has a solid mathematical foundation. The Hilbert-Huang transform was invented by Norden Huang around 20 years ago and is optimized to analyze aperiodic signals, nonlinear processes, and time-varying distortions. The Hilbert-Huang transform applied in analyses of modern power electronic systems has, as far as the author knows, not previously been explored. The subsequent sections will present the two methods and conduct an extensive analysis of the electrical waveform. The chapter will conclude with proposing a hypothesis of the origin of the distortions observed on the measured voltage waveform $v_{\mathrm{ac,m}}(t)$.

3.1 Power spectrum

The power spectrum shows the spectral characteristics of a signal by converting it from the time-domain to the frequency domain. The periodogram is a way to estimate the power spectrum. It has a long history and has been widely used since Schuster first introduced it in 1898.

The discrete Fourier transform can be used to define a periodogram of a time series expressing the power of each frequency component. The periodogram of

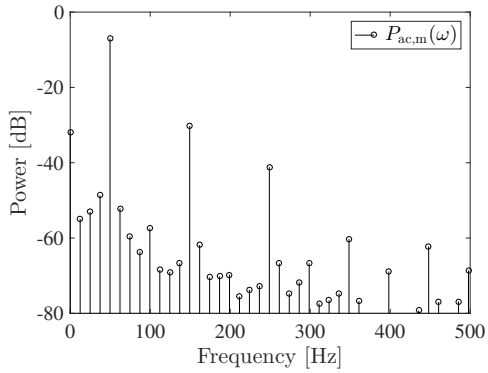

Figure 3.1: Power spectrum of $v_{\mathrm{ac,m}}(t)$. The spectrum is calculated using (3.1) where $N = 178$ and $F_s = 8.9$ KHz.

a sampled version of $v_{\mathrm{ac}}(t)$ is

$$P_{\mathrm{ac}}(\omega) = \frac{1}{N}\left|\sum_{n=0}^{N-1} v_{\mathrm{ac}}(nT_s)e^{-j\omega \cdot nT_s}\right|^2 \tag{3.1}$$

where ω is the angular frequency variable, T_s is the sampling period, n is the discrete time variable, and N is the total number of samples [10, pp 960-1046].

In figure 3.1 we have the power spectrum of $v_{\mathrm{ac,m}}(t)$. The power spectrum has a fundamental frequency ω_o, with odd harmonics of considerable amplitude. The power spectrum shows what harmonics are dominating. To gain a better understanding of the attributes of the signal, it will also be analyzed by using the Hilbert-Huang transform.

3.2 Hilbert-Huang transform

The notion of instantaneous frequency is new in power electronics [6]. We wanted to explore it on electrical systems to try to gain a better understanding of the cause of the distortions on the microgrid's voltage.

The instantaneous frequency concept has been applied in communication engineering for transmission of radio signals for about a century. However, it has been controversial as a tool to analyze physical processes. The definition's arbitrary phase-amplitude coupling is the primary reason for the controversy of its usefulness. Definitions and methods for an unambiguous understanding of instantaneous frequency for monocomponent signals, i.e. signals with only one local extremum for each zero crossing, have been discussed [11]. However, there has been few methods to define it for a multicomponent signal.

The relatively new Hilbert-Huang transform (HHT) aims at resolving these issues by providing a method to decompose any signal in monocomponents, and defining the instantaneous amplitude and frequency for these signals. For a general multicomponent signal $v(t)$ the HHT uses a method called the Empirical Mode Decomposition (EMD) to obtain the fewest monocomponents possible to describe it. These monocomponents are called intrinsic mode functions (IMFs). An IMF is defined as a function with one zero crossing between each local extrema. A flowchart of the Empirical Mode Decomposition algorithm is shown in figure 3.2. We can decompose voltage waveform $v(t)$ to a sum of IMFs on the form given in (3.2) by using the EMD algorithm.

$$v(t) = v_r(t) + \sum_{i=1}^{N_{\text{imf}}} v_i(t) \tag{3.2}$$

where $v_i(t)$ is IMF number i that $v(t)$ consist of, and $v_r(t)$ is the residue. The residue $v_r(t)$ is a monotonic function. The EMD uses a process called sifting to obtain monocomponents. One advantage of the EMD is the small amount of monocomponent it needs to describe a signal. N_{imf} is the total number of intrinsic mode functions and N_{imf} is restricted by (3.3) for most cases, according to Wu et. al. [12].

$$N_{\text{imf}} \leq \log_2 N \tag{3.3}$$

The naive implementation of the Empirical Mode Decomposition sets $N_{\text{imf}} = \log_2 N$ [7, 13]. Our implementation is different. We look at the difference between the sum of intrinsic mode function obtained during the sifting process and the original input signal $v(t)$. If the difference is a monotonic function or a monocomponent, the program will stop sifting. A general monocomponent can be written in the form

$$v_i(t) = V_i(t) \cdot \cos\big(\theta_i(t)\big) \tag{3.4}$$

The main controversy of the instantaneous frequency has been that $v_i(t)$ can be described with many different functions for $V_i(t)$ and $\theta_i(t)$. There exist several methods for defining and estimating the instantaneous amplitude $V_i(t)$ and phase $\theta_i(t)$ so they are unambiguous for the given method [14]. The two most prominent are described below.

3.2.1 Hilbert transform and the Bedrosian theorem

Early implementations of the Hilbert-Huang transform used the Hilbert transform to estimate the instantaneous amplitude and phase, hence the name Hilbert in Hilbert-Huang transform. The Hilbert transform of a given signal $v_i(t)$ is for all

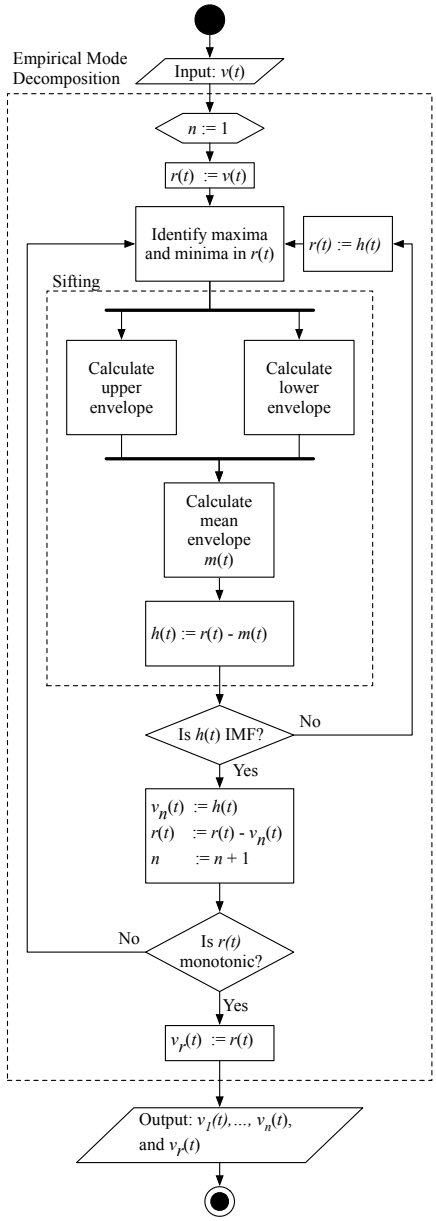

Figure 3.2: UML activity diagram of the Empirical Mode Decomposition (EMD) algorithm. The algorithm uses the input signal $v(t)$ and returns the fewest intrinsic mode functions (IMF) possible to describe it, $v_1(t)$, ..., $v_{N_{\mathrm{imf}}}(t)$, and a monotonic function $v_r(t)$. The upper envelope is defined by interpolating all local maxima using cubic spline interpolation. The same process is used on the local minima to get the lower envelope. The notation is intentionally different from the rest of the thesis to emphasize that this is internal signals in an algorithm.

practical use given by

$$\mathscr{H}\big(v_i(t)\big) = \frac{1}{\pi}\int_{\tau=-\infty}^{\infty}\frac{v_i(\tau)}{t-\tau}d\tau \tag{3.5}$$

$v_i(t)$ is used to define an *analytic signal* $z_i(t)$ [15] on the form given by

$$z_i(t) = v_i(t) + j\cdot\mathscr{H}\big(v_i(t)\big) = \check{V}_i(t)e^{j\check{\theta}_i(t)} \tag{3.6}$$

where $\check{V}_i(t)$ is the amplitude and $\check{\theta}_i(t)$ is the phase of $v_i(t)$ estimated using the analytic signal. Ideally, we want

$$\check{V}_i(t) = V_i(t) \tag{3.7}$$

and

$$\check{\theta}_i(t) = \theta_i(t). \tag{3.8}$$

There are mainly two limitations to this approach. The first is that the implementation of the Hilbert transform is not trivial as one needs an infinite integral. There are ways to estimate the Hilbert transform as one cannot get the real Hilbert transform of a physical signal, but these have restrictions. The second limitation is the Bedrosian Theorem that limits the situations where the instantaneous phase is meaningful in our application [16]. The Bedrosian theorem state that

$$\mathscr{H}\big(\check{V}_i(t)\cos\big(\check{\theta}_i(t)\big)\big) = \check{V}_i(t)\mathscr{H}\big(\cos\big(\check{\theta}_i(t)\big)\big) \tag{3.9}$$

only if the power spectrum of $\check{V}_i(t)$ and $\cos\big(\check{\theta}_i(t)\big)$ is disjoint, meaning that the power spectra of $\check{V}_i(t)$ and $\cos\big(\check{\theta}_i(t)\big)$ do not overlap[1]. We will use the normalized quadrature method due to these restrictions[2].

3.2.2 Normalized Quadrature method

There are several limitations to using the discrete Hilbert transform, as mentioned in the previous section. We therefore used Normalized Quadrature Method [17] to define and estimate instantaneous amplitude $V_i(t)$ and phase $\theta_i(t)$ of any monocomponent $v_i(t)$.

The first step of the Normalized Quadrature method is the normalization to define the amplitude. As an example, consider a given monocomponent $v(t)$ in the form

$$v(t) = \Big(\frac{1}{2}\cos(t) + 1\Big)\cdot\cos(5t) \tag{3.10}$$

It is shown in figure 3.3(a).

[1] Appendix A shows an example where these limitations are apparent.

[2] The Wu and Hue approach is also recommended for interested readers [17].

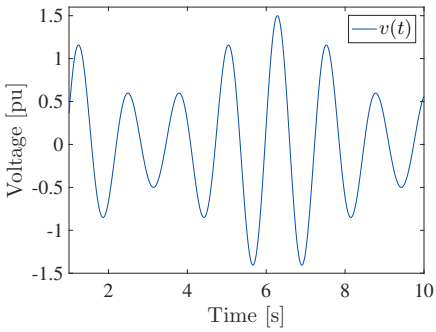

(a) Example waveform $v(t)$ for Normalized Quadrature method.

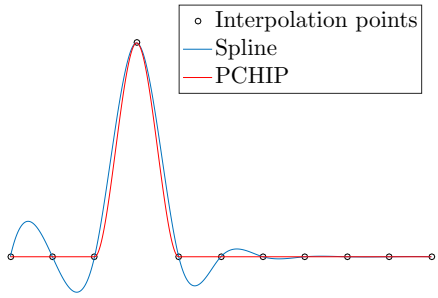

(b) Difference between cubic spline and Piecewise Cubic Hermite Interpolating Polynomial (PCHIP) interpolation.

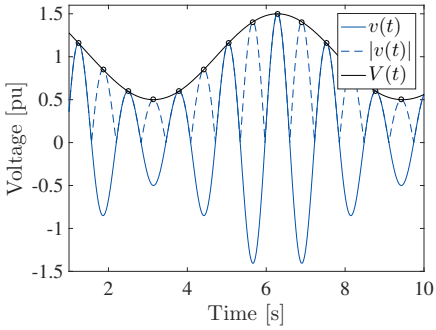

(c) Example of an estimation of the amplitude $a(t)$ using Normalized Quadrature method.

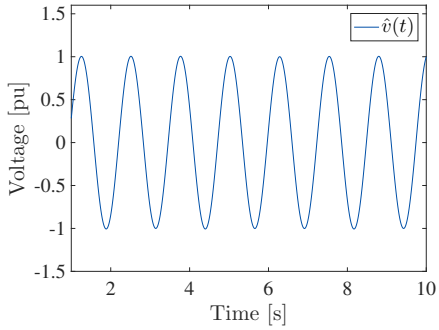

(d) Example of an estimation of the normalized $\hat{v}(t)$ using Normalized Quadrature method.

Figure 3.3: Example for figures for the Normalized Quadrature method.

The first step is to identify the local maxima of the absolute value of the signal, $|v(t)|$. The amplitude is defined by interpolating through these maxima. There are many different choices in interpolation methods for the amplitude. The most common used in this approach is Piecewise Cubic Hermite Interpolating Polynomial (PCHIP) [18]. The advantage of PCHIP in this application is that it can handle immediate changes in amplitude well. Figure 3.3(b) shows an example of the difference between PCHIP and cubic spline interpolation for a given dataset. The process of estimating the instantaneous frequency of the example waveform $v(t)$ is shown in figure 3.3(c).

Once the ampltidue $V(t)$ is defined, we define a new normalized signal

$$\hat{v}(t) = \frac{v(t)}{V(t)} = \cos\big(\theta(t)\big) \tag{3.11}$$

Figure 3.3(d) shows the normalized signal $\hat{v}(t)$. Note that $-1 \leq \hat{v}(t) \leq 1$ and that all local extrema are ± 1. The signal $\hat{v}(t)$'s phase can be obtained using the quadrature method. From the mathematical equivalent

$$\sin^2\big(\theta(t)\big) + \cos^2\big(\theta(t)\big) = 1 \tag{3.12}$$

we get that

$$\sin\big(\theta(t)\big) = k \cdot \sqrt{1 - \cos^2\big(\theta(t)\big)}, k = \begin{cases} -1 & \text{for } \frac{d\hat{v}(t)}{dt} > 0 \\ +1 & \text{otherwise} \end{cases}. \tag{3.13}$$

This means that we can calculate the phase

$$\theta(t) = \arctan \frac{k \cdot \sqrt{1 - \hat{v}^2}}{\hat{v}} \tag{3.14}$$

The phase $\theta(t)$ is used to obtain the frequency.

3.2.3 Instantaneous frequency

Once the phase $\theta(t)$ is obtained, the instantaneous angle frequency is defined as

$$\omega(t) = \frac{d\theta(t)}{dt} \tag{3.15}$$

where the instantaneous frequency is given by

$$f(t) = \frac{1}{2\pi} \cdot \omega(t) \tag{3.16}$$

The Hilbert Spectrum is a way to visualize the instantaneous frequency and amplitude as a function of time for all intrinsic mode functions of a signal [7]. For a given monocomponent on the form in (3.4), the Hilbert Spectrum is defined as

$$H_i(\omega, t) = \begin{cases} V_i(t) & \text{for } \omega = \omega_i(t) \\ 0 & \text{otherwise} \end{cases} \tag{3.17}$$

For a general multicomponent signal, the Hilbert Spectrum is defined as the sum of Hilbert Spectra of all the intrinsic mode functions obtained using the Empirical Mode Decomposition, as shown in (3.18).

$$H(\omega, t) = \sum_{i=1}^{N_{\text{imf}}} H_i(\omega, t) \tag{3.18}$$

3.2.4 Demonstration of the Hilbert-Huang transform

As an example of the HHT, we will consider a synthetic voltage $v(t)$ given by

$$v(t) = \cos(\omega_o t) + 0.03\cos(15\omega_o t) \tag{3.19}$$

It has a fundamental frequency ω_o and one harmonic $15\omega_o$ and is shown in figure 3.4(a). By applying the Empirical Mode Decomposition on $v(t)$, it is decomposed into the two monocomponents $v_1(t)$ and $v_2(t)$ so that

$$v(t) = v_1(t) + v_2(t). \tag{3.20}$$

$v(t)$'s IMFs are shown in figure 3.4(b). The Hilbert Spectrum of $v(t)$ is shown in figure 3.5. The blue line at the top of the Hilbert Spectrum depicts $v_2(t)$ and the dark red $v_1(t)$. The Hilbert Spectrum has some end effects. If the end-effects are discarded, then the blue line at the top $v_2(t)$ of the Hilbert spectrum will have a constant frequency and amplitude at $f_2(t) = 750.00$ Hz and $a_2(t) = -30.73$ db $= 0.02907$. $v_1(t)$ will also have constant frequency and amplitude if the end-effects are discarded. The frequency of $v_1(t)$ is $f_1(t) = 50$ Hz and the amplitude is $a_1(t) = -0.25$ dB $= 0.97$.

3.2.5 Hilbert-Huang transform of measured voltage waveform

The Hilbert-Huang transform of $v_{\text{ac,m}}(t)$, shown in figure 2.2, is used to gain a better understanding of the origin of the distortions in the inverter discussed in the beginning of this chapter. The voltage waveform $v_{\text{ac,m}}(t)$ is decomposed into two intrinsic mode functions, $v_{\text{ac,md}}(t)$ and $v_{\text{ac,mg}}(t)$, using the Empirical Mode Decomposition so that

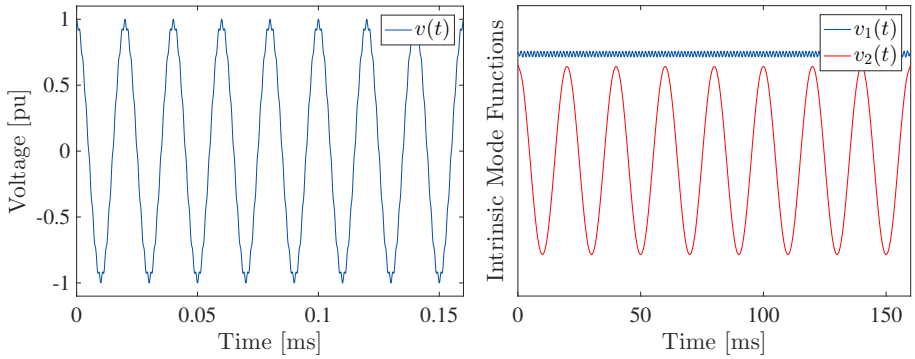

(a) Voltage $v(t)$ given by (3.19).

(b) Voltage $v(t)$ decomposed into intrinsic mode functions $v_1(t)$ and $v_2(t)$.

Figure 3.4: Example of a signal and its decomposition using Empirical Mode Decomposition.

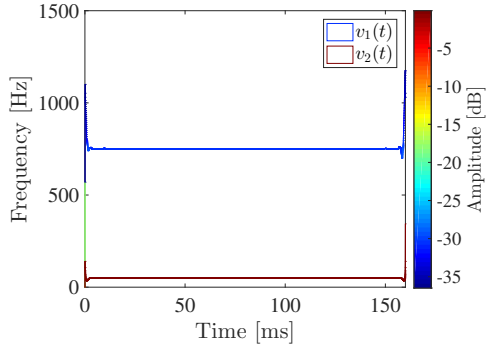

Figure 3.5: Hilbert spectrum of $v(t)$.

$$v_{\mathrm{ac,m}}(t) = v_{\mathrm{ac,md}}(t) + v_{\mathrm{ac,mg}}(t) \tag{3.21}$$

The subscript d stand for distortions and g for the grid. The intrinsic mode functions are shown in figure 3.6(a). The first intrinsic mode function, $v_{\mathrm{ac,md}}(t)$ is shown as the green and blue part in the Hilbert spectrum and is centered mostly between 500 Hz and 1500 Hz. The red line at the bottom corresponds to the grid component $v_{\mathrm{ac,mg}}(t)$. There is a severe limitation on the accuracy of the instantaneous frequency of $v_{\mathrm{ac,md}}(t)$ due to discrete differentiation. As shown in (3.15), the instantaneous frequency is defined as

$$\omega(t) = \frac{d\theta(t)}{dt} = \lim_{\Delta t \to 0} \frac{\theta(t + \Delta t) - \theta(t)}{\Delta t} \tag{3.22}$$

We use Forward Euler (FE) [19] when calculating the derivative of phase $\theta(t)$ to obtain the instantanious frequency $\omega(t)$. The method Forward Euler approximate

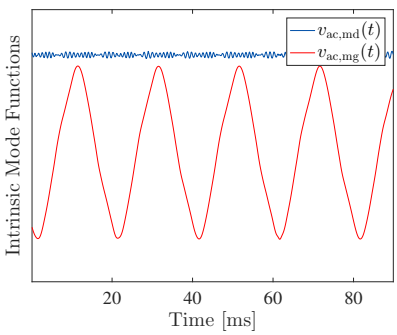

(a) Measured voltage $v_{\mathrm{ac,m}}(t)$ decomposed into intrinsic mode functions $v_{\mathrm{ac,md}}(t)$ and $v_{\mathrm{ac,mg}}(t)$.

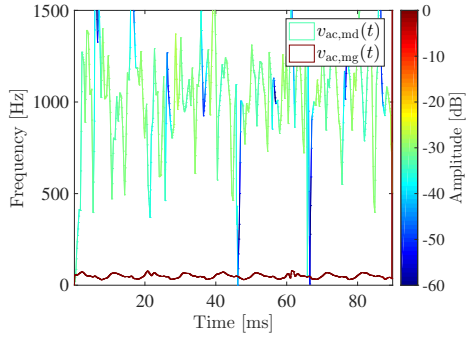

(b) Hilbert spectrum of $v_{\mathrm{ac,m}}(t)$.

Figure 3.6: Hilbert-Huang transform of $v_{\mathrm{ac,m}}(t)$.

that $\Delta t \approx T_s$ as well as using discrete time where $t = n \cdot T_s$. This means that we can approximate the instantanious frequency as

$$\omega(t) = \omega(n \cdot T_s) \approx F_s\Big(\theta\big((n+1) \cdot T_s\big) - \theta(n \cdot T_s)\Big) \tag{3.23}$$

This is true as long as the instantaneous frequency is

$$\omega(t) \ll 2\pi F_s \tag{3.24}$$

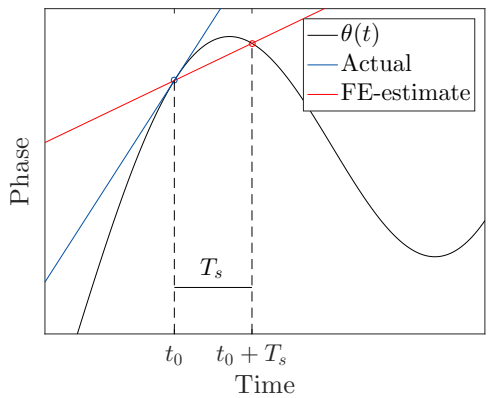

Figure 3.7: Example of the effects on the estimate of the instantaneous frequency when experiencing high frequency to sampling rate ratio. The blue line depicts the tangent for the actual instantaneous frequency in $t = t_0$. The red is an estimate of the instantaneous frequency when using Forward Euler without sufficiently high sampling rate F_s.

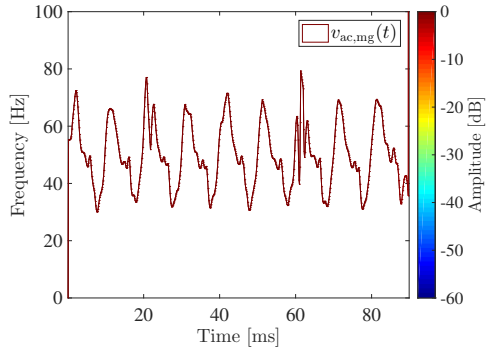

Figure 3.8: Hilbert spectrum of $v_{\mathrm{ac,mg}}(t)$.

where F_s is the *sampling frequency* and is given by $F_s = \frac{1}{T_s}$. Simulations of cases shows good results as long as $\omega(t) < 0.02 \cdot 2\pi F_s$. This is satisfied for $v_{\mathrm{ac,mg}}(t)$. For $v_{\mathrm{ac,md}}(t)$ this is not the case. Figure 3.7 shows an example of the effect when the assumption in (3.24) does not hold. From the difference between the blue tangent and the red line in the figure, it is clear that the Forward-Euler estimated instantaneous frequency is far from the actual instantaneous frequency. It is possible to overcome this problem [20], but these solutions have not been implemented during this project. The monocomponent $v_{\mathrm{ac,md}}(t)$ containing the high-frequency distortions will therefore not be analyzed further.

Figure 3.8 shows $v_{\mathrm{ac,mg}}(t)$'s Hilbert Spectrum in greater detail. Its frequency has a semi-periodic behavior with repetition every 10 ms. The grid-component also has some interesting non-periodic behavior. The magnitude of the frequency variations is also relatively large, varying from 30 Hz to 80 Hz, with a mean frequency of 50 Hz.

3.3 Suggested hypothesis for the root of distortions

To find a semiperiodic repetition on the grid frequency's monocomponent $v_{\mathrm{ac,mg}}(t)$ with frequency fluctuations of 10 ms (100 Hz) was unexpected for the author. It led the author to suspect that the distortion originates in the dc current $i_d(t)$. By following the model in figure 2.1 and assuming that no energy is stored in the filters and a linear load R_{load} we get that the instantaneous power input $P_d(t)$ is equal to the instantaneous ac power output $P_{\mathrm{ac}}(t)$ so that

$$P_d(t) = P_{\mathrm{ac}}(t) \tag{3.25}$$

We also assume an almost pure sinusoidal output voltage so that

$$v_{\mathrm{ac}}(t) \approx V_{\mathrm{ac}} \sin(\omega_o t) \tag{3.26}$$

Since the load is assumed to be linear the current will be

$$i_{\mathrm{ac}}(t) \approx I_{\mathrm{ac}} \sin(\omega_o t) \tag{3.27}$$

By following the argumentation of Mohan at. al [21, p. 214] we get that under the assumption that no energy is stored in the filters, we have

$$P_d(t) = v_{\mathrm{ac}}(t) \cdot i_{\mathrm{ac}}(t) = V_{\mathrm{ac}} I_{\mathrm{ac}} \sin(\omega_o t - \phi_i) \sin(\omega_o t) \tag{3.28}$$

therefore

$$i_d(t) = \frac{V_{\mathrm{ac}} I_{\mathrm{ac}}}{V_d} \cos\phi_i - \frac{V_{\mathrm{ac}} I_{\mathrm{ac}}}{V_d} cos(2\omega_o t - \phi_i) \tag{3.29}$$

This can be rewritten as

$$\begin{aligned} i_d(t) &= I_d + \tilde{i}_d(t) \\ &= I_d + \tilde{I}_d \cos(2\omega_o t) \end{aligned} \tag{3.30}$$

Equation (3.29) assumes that $V_d \gg \tilde{v}_d(t)$. Figure 3.9 shows a Thévenin equivalent of the dc power supply seen from the output of the boost controller in figure 2.1. The dc voltage supply $v_d(t)$ will be described by

$$\begin{aligned} v_d(t) &= V_s - i_d(t) \cdot R_s \\ &= V_s - R_s \cdot I_d + R_s \tilde{I}_d \cos(2\omega_o t) \\ &= V_d + \tilde{V}_d \cos(2\omega_o t) \end{aligned} \tag{3.31}$$

where V_s is the constant dc power supply, R_s is the power supply's internal resistance, $V_d = V_s - R_s \cdot I_s$, and $\tilde{V}_d = R_s \cdot \tilde{I}_d$.

This led us to suggest that the distortions in $v_{\mathrm{ac,m}}(t)$ originated from the dc voltage $v_d(t)$, because of the $2\omega_o$ component in (3.31), and not from nonlinear loads.

Following the principle of falsifiability, this hypothesis will be discarded if a 100 Hz oscillation on the dc bus does not result in a 10 ms oscillation on the instantaneous frequency of the 50 Hz grid component in the simulation or analytic models described in the next sections [22]. We aim to minimize a positive bias that researchers (and students) often experience towards confirming instead of challenging initial hypothesis by explicitly stating an apparent condition for falsifiability [23].

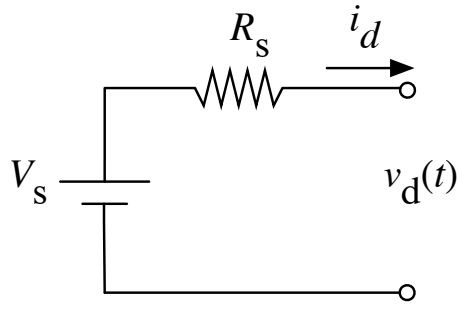

Figure 3.9: Thévenin equivalent of dc power supply.

Chapter 4

Modeling and analytical investigation of the hypothesis

In the previous chapter, we presented some voltage measurements and ways to interpret them. We will use these interpretations in this section to examine the system behind the microgrid. We suspected that the origin of the distortions originated from the dc bus $v_d(t)$ amplified by the controller, as mentioned in section 3.3. To test this hypothesis, a model of the system is necessary. We have not been able to get a detailed model from the manufacturer, so we assumed a typical microgrid setup and controller. Therefore, the inverter controller used in this thesis is based on a standard PV inverter controller [24, 25]. The frequency and phase-shift synchronization are not accounted for in this report as the microgrid is islanded. The controller's task is to monitor and correct the output voltage $v_{\text{ac}}(t)$. The controller's main blocks are a proportional-integral (PI) controller and a Resonant Controller (RC). A detailed model of the microgrid is shown in figure 4.1.

The dc voltage $v_d(t)$ is converted to ac, $v_{\text{ac}}(t)$, by using a dc/ac inverter. The inverter is a steady-state single bridge inverter based on pulse-width modulation (pwm) [21] with a low-pass filter. The inverter has a controller that uses ω_o, $v_d(t)$ and $i_{\text{ac}}(t)$ to control $v_{\text{ac}}(t)$ so that ideally, the ac output voltage should always be given on the form in (2.1). $v_{\text{ac}}(t)$ is adjusted by $v_{\text{control}}(t)$. By assuming an optimal dc/ac inverter and filters, $v_{\text{ac}}(t)$ will be

$$v_{\text{ac}}(t) \propto v_{\text{control}}(t). \tag{4.1}$$

A previous study lead us to believe that the distortions originate in an oscillation on the dc bus [6] as discussed in section 3.3. By following the argumentation in

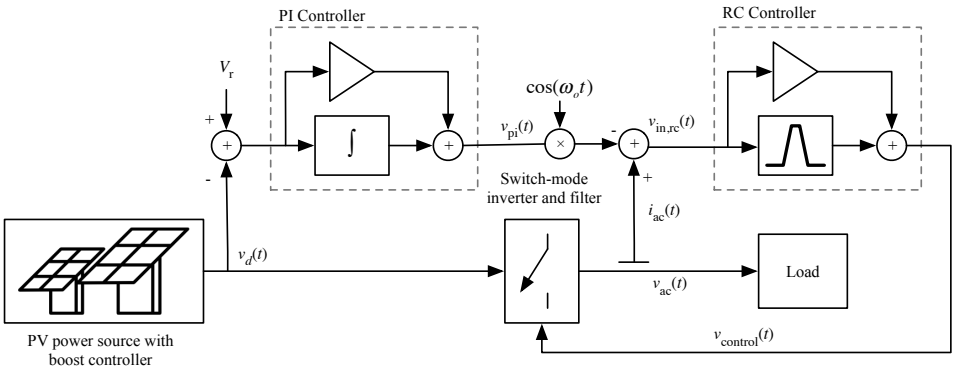

Figure 4.1: High level model of the microgrid investigated in this thesis.

section 3.3; if the load is a resistance, the dc voltage can be modelled as

$$v_d(t) = V_d + \tilde{v}_d(t) = V_d + \tilde{V}_d \cos(2\omega_o t). \tag{4.2}$$

In the controller, the dc voltage, $v_d(t)$ is compared with a predefined reference dc voltage V_r and results in a correction signal

$$v_e(t) = V_r - v_d(t). \tag{4.3}$$

As mentioned, the controller has two main components. The purpose of the proportional-integral controller (PI) is to maintain a stable output amplitude of $v_{\mathrm{ac}}(t)$ while there are slow-varying changes in the dc voltage $v_{\mathrm{d}}(t)$.

We assume a stable boost controller so that the correction signal V_r is equal to V_d. The proportional-integral controller (PI) uses the correction signal $v_e(t)$ as an input. Since the PI controller is a linear operation, it will only alter the amplitudes and phases and not any frequency value of $v_d(t)$, resulting in an output of the PI controller

$$v_{\mathrm{pi}}(t) = A\cos(2\omega_o t - \phi) \tag{4.4}$$

where A and ϕ are the resulting amplitude and phase after the PI controller. The resulting signal $v_{\mathrm{pi}}(t)$ out of the PI controller $v_{\mathrm{pi}}(t)$ is multiplied with a sinusoidal signal. It is then compared with a the ac current $i_{\mathrm{ac}}(t)$ so that

$$v_{\mathrm{in,rc}}(t) = R_k i_{\mathrm{ac}}(t) - v_{\mathrm{pi}}(t) \cdot \cos(\omega_o t) \tag{4.5}$$

R_k is a constant to scale $i_{\mathrm{ac}}(t)$. The optimal condition for the PI controller is when $v_{\mathrm{pi}}(t)$ is constant or slow varying. $v_{\mathrm{in,rc}}(t)$ is used as the input to a Resonant Controller (RC). The Resonant Controller is a band-amplifier and is used to ensure

a stable grid-frequency. As mentioned at the beginning of section 3, we assume a resistive load. This gives us that

$$v_{\text{ac}}(t) = R_{\text{load}} \cdot i_{\text{ac}}(t). \tag{4.6}$$

This assumption, together with the expression for output of the RC controller $v_{\text{pi}}(t)$ given by (4.4) and the input to the resonant controller $v_{\text{in,rc}}(t)$ in (4.5) we get that

$$\begin{aligned} v_{\text{in,rc}}(t) &= -A\cos(2\omega_o t - \phi) \cdot \cos(\omega_o t) + B' \cdot v_{\text{ac}} \\ &= -\frac{A}{2}\big(\cos(\omega_o t - \phi) + \cos(3\omega_o t - \phi)\big) + B' \cdot v_{\text{ac}}(t) \end{aligned} \tag{4.7}$$

where B' is a constant to scale $v_{\text{ac}}(t)$. The Resonant Controller is a linear band amplifier that let all frequencies pass, but amplifies the grid frequency ω_o. Its purpose is to maintain a stable grid-frequency. Because the RC controller only changes amplitudes and phases we get a control voltage $v_{\text{control}}(t)$ given by

$$\begin{aligned} v_{\text{control}}(t) = C_1' \cos\big(\omega_o t - \phi_1'\big) + C_2' \cos\big(3\omega_o t - \phi_2'\big) \\ + B \cdot v_{\text{ac}}(t) \end{aligned} \tag{4.8}$$

where C_1', C_2', B, ϕ_1', and ϕ_2' are constants determined by $v_{\text{in,rc}}(t)$ through the RC controller. By assuming that the fundamental frequency component of $v_{\text{ac}}(t)$ has much larger amplitude than its harmonics, we can approximate that the effect of the feedback from the ac side $B \cdot v_{\text{ac}}(t)$ through the RC controller will be given by

$$v_{\text{feedback}}(t) = v_{\text{ac}}(t) * h_{\text{rc}}(t) \approx C_{\text{ac}} \cos(\omega_o t + \phi_{\text{ac}}) \tag{4.9}$$

where $h_{\text{rc}}(t)$ is the impulse response of the RC controller, and C_{ac} and ϕ_{ac} are constant determined by $B \cdot v_{\text{ac}}(t)$ through the RC controller. We can put (4.9) into (4.8) so that

$$\begin{aligned} v_{\text{control}}(t) = C_1' \cos\big(\omega_o t - \phi_1'\big) + C_2' \cos\big(3\omega_o t - \phi_2'\big) \\ + C_{\text{ac}} \cos(\omega_o t + \phi_{\text{ac}}). \end{aligned} \tag{4.10}$$

Because $v_{\text{control}}(t)$ is proportional to $v_{\text{ac}}(t)$ as stated in (4.1), we get that

$$v_{\text{ac}}(t) = C_1 \cos(\omega_o t - \phi_1) + C_2 \cos(3\omega_o t - \phi_2) \tag{4.11}$$

where C_1, C_2, ϕ_1, and ϕ_2 are constants determined by $v_{\text{control}}(t)$ through the dc/ac inverter. Note that the distortions in (4.11) is a sum of two frequency components, but is caused by a multiplication operator in the controller.

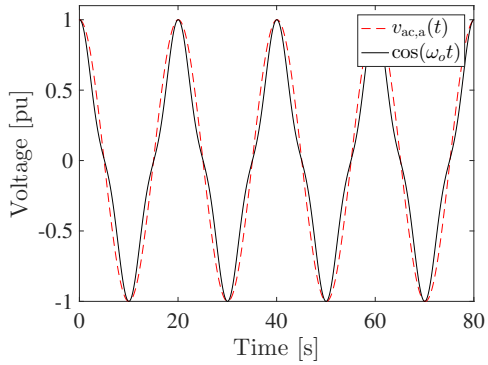

Figure 4.2: $v_{\mathrm{ac,a}}(t)$ from (4.11) against an ideal ac voltage waveform as in (2.1).

4.1 Analytical investigation of the hypothesis

In the previous chapters, we have examined measured voltage data $v_{\mathrm{ac,m}}(t)$ and made a mathematical model to describe the microgrid system. In this section, we will look at the mathematical equations describing the model, test some of the assumptions, and relate them to the measured data to test the hypothesis that the origin of the distortion comes from the dc bus, as presented in section 3.3. Because we now have a mathematical expression of the system describing the microgrid in figure 4.1, we may compare the results from the analytical model with the data measured on the microgrid in Bhutan. A detailed expression of $v_{\mathrm{ac}}(t)$ on the form in (4.11) is used to get the values for C_1, C_2, ϕ_1, and ϕ_2 based on the controller's tuning. Reasonable values of the constant in the controller is chosen based on discussions with, and a model provided by, Dr. Jon Are Suul in Department of Electric Power Engineering. The subscript a is added to $v_{\mathrm{ac}}(t)$ to show that it is analytical. Table 4.1 shows the values chosen. The resulting waveform is shown as the black line in figure 4.2. It is compared with an ideal voltage waveform on the from given by (2.1), shown in red.

4.1.1 Power spectrum and pulse-width modulation

The power spectrum of $v_{\mathrm{ac}}(t)$ on the form given in (4.11) is given by

$$P_{\mathrm{ac,a}}(\omega) = |C_1|^2\delta(\omega - \omega_o) + |C_2|^2\delta(\omega - 3\omega_o) \tag{4.12}$$

where δ is the *Dirac delta function* [26, p. 242]. $P_{\mathrm{ac,a}}(\omega)$ is shown in figure 4.3. The power spectrum has a fundamental frequency ω_o, and one harmonic at $3\omega_o$. The power spectrum of the measured voltage waveform $v_{\mathrm{ac,m}}(t)$ in figure 3.1's two most powerful frequency components were also at ω_o and $3\omega_o$, but $v_{\mathrm{ac,m}}(t)$ also contained a notable harmonic at $5\omega_o$. A possible explanation of the $5\omega_o$ frequency

Table 4.1: Microgrid model parameters.

DC power supply		
Line Impedance	R_s	0.1 Ω
Voltage	V_d	400 V
Current	I_d	22 A
AC power consumption		
Load Impedance	R_{load}	7 Ω
Voltage	V_{ac}	230 V_{rms}
Proportional-integral controller		
Proportional coefficient	K_p	2
Integral coefficient	K_i	20
Proportional-resonant controller		
Proportional coefficient	C_p	1
Resonant coefficient	C_i	5

component in the measured voltage's $v_{\text{ac,m}}(t)$ power spectrum is effects caused by the pulse-width modulation. This explanation can be strengthened further by the fact that the pulse-width modulation mainly consists of odd harmonics.

We will, therefore, temporarily disregard the assumption stated in (4.1) that states that the ac voltage $v_{\text{ac}}(t)$ is proportional to the control signal $v_{\text{control}}(t)$ to test the statement above. A numerical Matlab model of a pulse-width modulated signal based Mohan et. al [21, pp. 212–215] is designed so we could generate $v_{\text{pwm}}(t)$ numerically based on the expression of $v_{\text{control}}(t)$ in (4.8). The calculations for a detailed expression of $v_{\text{control}}(t)$ is shown in appendix B. The parameters were estimated using table 4.1, but we sat $B = 0$ in this analysis as we focus on the oscillations from the dc voltage through the controller.

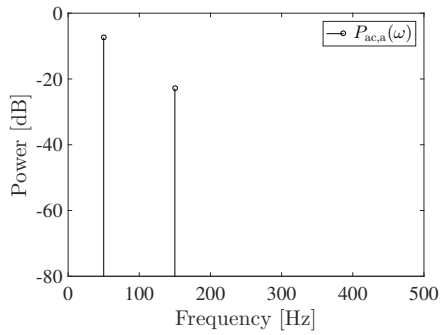

Figure 4.3: Power spectrum of $v_{\text{ac,a}}(t)$.

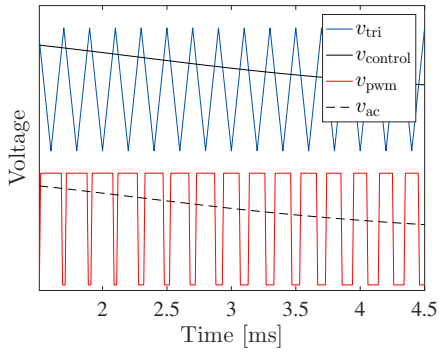

Figure 4.4: Numerical estimation of the pwm effect on $v_{\text{ac,a}}(t)$.

The pwm voltage $v_{\text{pwm}}(t)$ is created by comparing $v_{\text{control}}(t)$ with a synthetic triangular signal $v_{\text{tri}}(t)$. $v_{\text{tri}}(t)$ has a fundamental frequency of 5 KHz in our Matlab model. The pwm voltage from the inverter $v_{\text{pwm}}(t)$ is given by

$$v_{\text{pwm}}(t) = \frac{1}{2}\begin{cases} +V_d, & \text{if } v_{\text{control}}(t) > v_{\text{tri}}(t) \\ -V_d, & \text{if } v_{\text{control}}(t) \leq v_{\text{tri}}(t) \end{cases} \tag{4.13}$$

and is shown in figure 4.4. The pwm voltage $v_{\text{pwm}}(t)$ is then filtered using an inductor-based first order low-pass filter as shown in figure 4.5. The filter was simulated with a digital low pass filter with a transfer function

$$H_{\text{lp}}(s) = \frac{\omega_c}{s + \omega_c} \tag{4.14}$$

We can now express the pwm corrected ac voltage

$$v_{ac,n}(t) = v_{\text{pwm}}(t) * h_{\text{lp}}(t) \tag{4.15}$$

where $h_{\text{lp}}(t)$ is the impulse response of the filter in (4.14). The subscript n is added to v_{ac} to show that it is numerical corrected for pwm and filter effects. Figure 4.6 shows the power spectrum of $v_{ac,n}(t)$. All odd harmonics of ω_o has a considerable amplitude, and the shape is similar to that of $P_{\text{ac,m}}(\omega)$ as shown in figure 3.1.

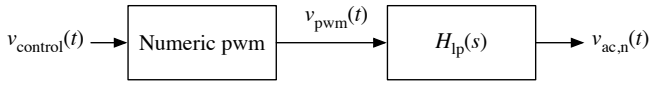

Figure 4.5: Pulse-width modulated voltage $v_{\text{pwm}}(t)$ generated by comparing a generated triangular signal $v_{\text{tri}}(t)$ with $v_{\text{control}}(t)$.

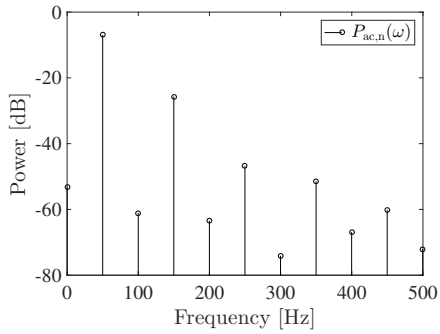

Figure 4.6: Power spectrum of $v_{\mathrm{ac,n}}(t)$. The spectrum is calculated using (3.1) where $N = 2000$ and $F_s = 100$ KHz.

4.1.2 Hilbert spectrum

In figure 3.8, the Hilbert spectrum of $v_{\mathrm{ac,mg}}(t)$ shows a 10 ms oscillation in the instantaneous grid frequency of $v_{\mathrm{ac,m}}(t)$. It is therefore expected to find the same 10 ms oscillation in the instantaneous frequency of the analytical expression.

The analytical expression of $v_{\mathrm{ac}}(t)$ given by (4.11) satisfies the requirements for an intrinsic mode function for all reasonable variables for tuning of the controller, so the Empirical Mode Decomposition is not needed. This means that we can write $v_{\mathrm{ac}}(t)$ on the form

$$v_{\mathrm{ac}}(t) = V_{\mathrm{ac}}(t) \cdot \cos\left(\theta_{\mathrm{ac}}(t)\right) \tag{4.16}$$

where $v_{\mathrm{ac}}(t)$ only has one zero-crossing per local extrema.

The Hilbert spectrum of $v_{\mathrm{ac}}(t)$ using the same tuning as the previous chapter is shown in figure 4.7. From the figure it is clear that the frequency changes over time. The instantaneous frequency should ideally be $\omega_{ac}(t) = \omega_o$. We approximated

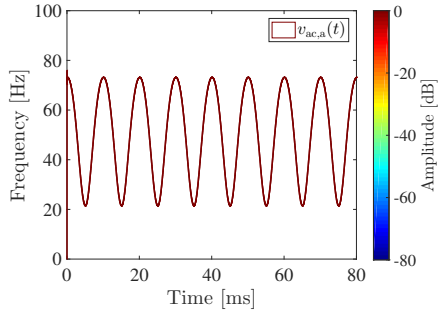

Figure 4.7: Hilbert spectrum of $v_{\mathrm{ac,a}}(t)$.

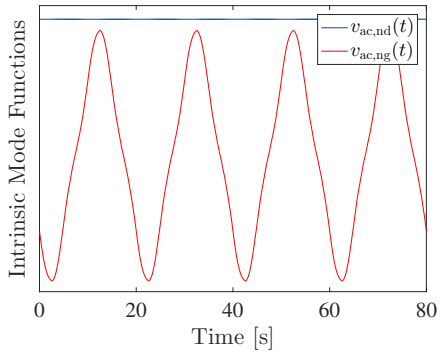

Figure 4.8: The intrinsic mode functions describing $v_{\mathrm{ac,n}}(t)$.

$\omega_{\mathrm{ac}}(t)$ to

$$\omega_{\mathrm{ac}}(t) \approx \omega_o + \epsilon \cos(2\omega_o t) \tag{4.17}$$

with an error of less than 11.7 %. The constant ϵ corresponds to the magnitude of the oscillating frequency. The same periodic behaviour on $\omega_{\mathrm{ac}}(t)$ with the 10 ms cycles is also found in $v_{\mathrm{ac,m}}(t)$'s Hilbert spectra, as discussed in section 3.2.5.

This means that the analytical expression shows both the 10 ms oscillation on the instantaneous frequency in the Hilbert Spectrum, and the most powerful frequency components in the Power spectrum found on the measured voltage waveform $v_{\mathrm{ac,m}}(t)$ in section 3.1. This indicates that the hypothesis in section 3.3 may describe the distortions observed on $v_{\mathrm{ac,m}}(t)$.

The analytical model has several simplifications and assumptions. We will therefore make a Hilbert spectrum of the electrical waveform $v_{\mathrm{ac,n}}(t)$ when compensating from pwm and filtering.

Hilbert spectrum corrected for pwm effects

We will now use the Hilbert spectrum to analyze the numerically estimated voltage waveform $v_{\mathrm{ac,n}}(t)$ discussed in section 4.1.1 to verify that the 10 ms oscillation still occurs when the voltage waveform is affected by pwm and filtering. The waveform $v_{\mathrm{ac,n}}(t)$ is decomposed into two intrinsic mode functions (IMF) as shown in section 3.2.5 so that

$$v_{\mathrm{ac,n}}(t) = v_{\mathrm{ac,nd}}(t) + v_{\mathrm{ac,ng}}(t) \tag{4.18}$$

Figure 4.8 shows the two IMFs. The Hilbert spectrum of $v_{\mathrm{ac,n}}(t)$ is shown in figure 4.9(a). The monocomponent $v_{\mathrm{ac,nd}}$'s frequency struggles with a high frequency to sampling frequency ratio as discussed in section 3.2.5. We will, therefore, discard $v_{\mathrm{ac,nd}}(t)$ from any further analysis. Figure 4.9(b) shows $v_{\mathrm{ac,ng}}(t)$'s Hilbert spec-

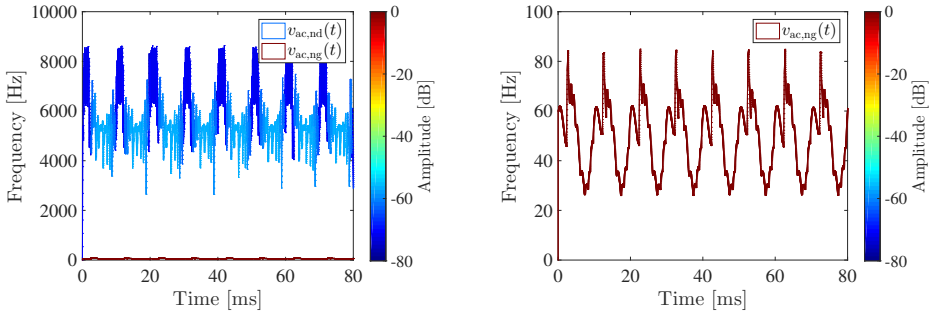

(a) Hilbert spectrum of $v_{\mathrm{ac,n}}(t)$.

(b) Hilbert spectrum of $v_{\mathrm{ac,ng}}(t)$.

Figure 4.9: Hilbert spectra of $v_{\mathrm{ac,n}}(t)$.

trum in greater detail. It has a 10 ms repetition similar to figure 4.7, but it is more distorted. The analytical $v_{\mathrm{ac,a}}(t)$ and numerical $v_{\mathrm{ac,n}}$'s instantaneous frequencies both show the same 10 ms pattern observed on $v_{\mathrm{ac,m}}(t)$.

In the next chapter, we will use a Simulink simulation to test the hypothesis further.

Chapter 5

Validation of the hypothesis with simulation

In the previous chapters, we have investigated and analyzed the voltage measurements from the microgrid described in section 3 and compared it with a mathematical model from section 4 to test a hypothesis about the origin of the distortion. A simulation of the microgrid system based on the model in section 4 is used to verify these findings.

The simulation is implemented using Simulink. The simulation is tailored to show as real conditions as possible and is simulating non-ideal conditions with considerable line impedance and a resistive load as suspected in the microgrid where we

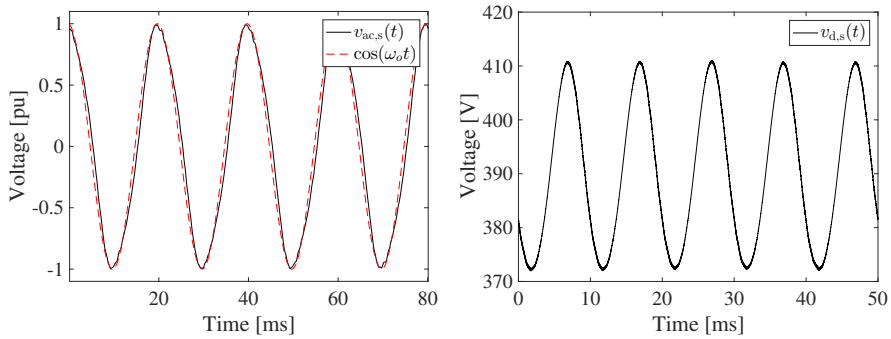

(a) Simulated output from an dc/ac inverter, $v_{\mathrm{ac,s}}(t)$ against an ideal cosine.

(b) 100 Hz oscillations shown on dc bus $v_{d,s}(t)$, as expected from section 3.3.

Figure 5.1: Simulated $v_{\mathrm{ac,s}}(t)$ and $v_{d,s}(t)$.

did the measurements. The parameters for the simulation were the same as used for the analytical investigations in section 4.1 and can be found in table 4.1. Figure 5.6 shows a Simulink block diagram of the simulation.

The letter s will be added in subscript to variables to mark that they are found using the simulation. The ac voltage $v_{\mathrm{ac,s}}(t)$ is shown in figure 5.1(a). $v_{\mathrm{ac,s}}(t)$ is distorted compared with a pure sinusoidal waveform with frequency ω_o, yet in a different way than v_{ac} in figure 4.2. Unlike the analytical expression of v_{ac}, the ac voltage $v_{\mathrm{ac,s}}(t)$ curves towards the right compared with a pure sinusoidal signal (red). It also contains ripples that are most probably caused by the distortions by the inverter's pulse-width modulation that is not properly filtered by the low-pass filter as discussed in the previous chapter. The simulation also found the 100 Hz oscillation on the dc bus $v_{d,s}(t)$ as shown in figure 5.1(b).

5.1 Power spectrum

The power spectrum of $v_{\mathrm{ac,s}}(t)$ is given in figure 5.2. The power spectrum of $v_{\mathrm{ac,s}}(t)$ is dominated by odd harmonics, like the power spectra of the measured waveform $v_{\mathrm{ac,m}}$ and the analytical investigation of $v_{\mathrm{ac,a}}(t)$ in section 3.1 and 4.1.1. The 50 Hz and 150 Hz are most prominent in all three investigations.

5.2 Hilbert spectrum

The ripples make $v_{\mathrm{ac,s}}(t)$ a multicomponent signal, so it is decomposed into two intrinsic mode functions (IMFs) using EMD with zero residue so that

$$v_{\mathrm{ac,s}}(t) = v_{\mathrm{ac,sd}}(t) + v_{\mathrm{ac,sg}}(t) \tag{5.1}$$

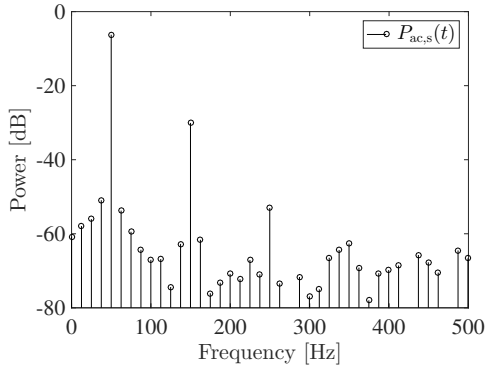

Figure 5.2: Power spectrum of $v_{\mathrm{ac,s}}(t)$. The spectrum is calculated using (3.1) where $N = 20$ K and $F_s = 1$ MHz.

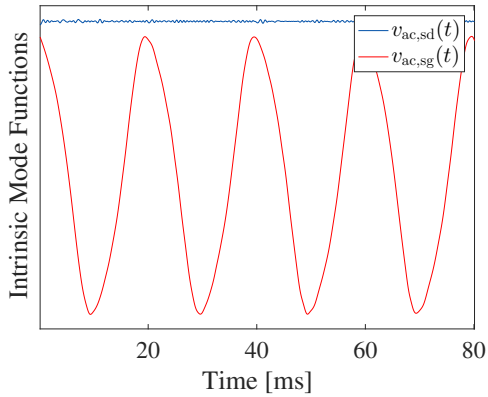

Figure 5.3: The simulated $v_{\mathrm{ac,s}}$'s intrinsic mode functions.

The first IMF $v_{\mathrm{ac,sd}}(t)$ contain the high-frequency distortions most probably caused by non-ideal filtering and the pulse-width modulation as discussed in the previous chapter. The second IMF $v_{\mathrm{ac,sg}}(t)$ is the grid component. The IMFs are shown in figure 5.3. The IMFs' instantaneous amplitude and frequency were calculated using the normalized quadrature method, as described in section 3.2.2. They are shown in the Hilbert spectrum in figure 5.4. The high frequency component $v_{\mathrm{ac,sd}}(t)$ is changing so rapidly that it is experiencing the issues with discrete differentiation as described in section 3.2.5. This IMF will therefore not be further analyzed.

The Hilbert spectrum of the grid component $v_{ac,sg}(t)$ is shown in greater detail in figure 5.5. The instantaneous amplitude is constant, and the instantaneous frequency has a 10 ms oscillation and some oscillatory behavior. This 10 ms behavior did also occur on the analytic model in section 4 and the measured voltage data

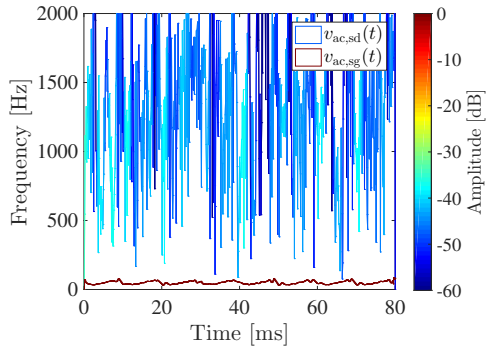

Figure 5.4: Hilbert spectrum of $v_{\mathrm{ac,s}}(t)$.

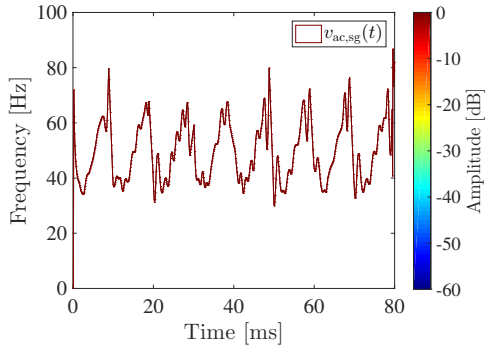

Figure 5.5: Hilbert spectrum of $v_{\mathrm{ac,s}}(t)$.

$v_{\mathrm{ac,m}}(t)$'s Hilbert spectra in section 3.2. The falsification condition of the hypothesis is therefore not fulfilled.

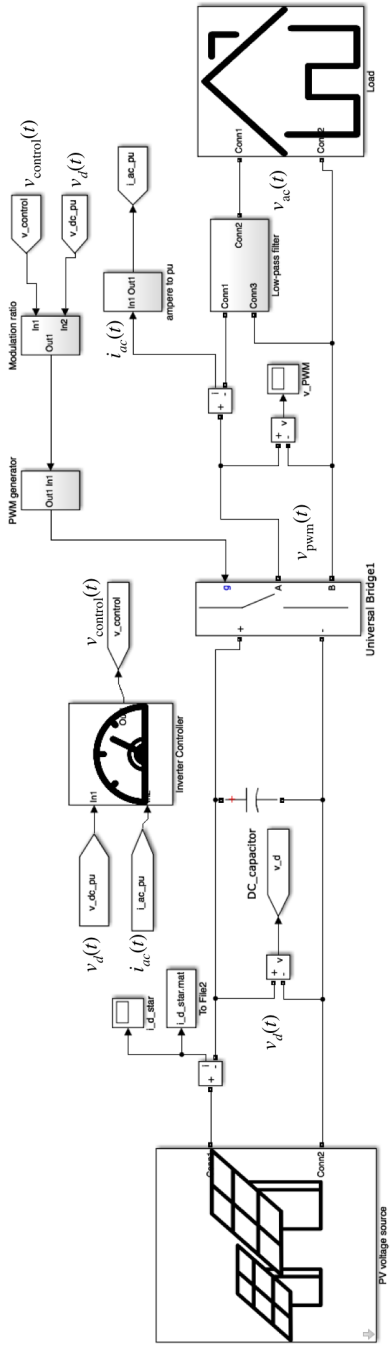

Figure 5.6: Simulink schematics of the main blocks of the microgrid simulation.

Chapter 6

Positive feedback cascading effect as cause of distortion

We have so far examined a hypothesis where we state that the origin of the distortion on the ac voltage is a 100 Hz oscillation on the dc bus that originates from feedback from the ac side, as indicated in section 3.3. In this chapter, we will informally investigate a generalization of the origin of the distortion based on a harmonic analysis. Let's consider the microgrid model in figure 4.1.

By grouping the subsystems in $h_1(t)$ and $h_2(t)$ as shown in figure 6.1, we can abstract the system to two linear operations $h_1(t)$ and $h_2(t)$, one multiplication,

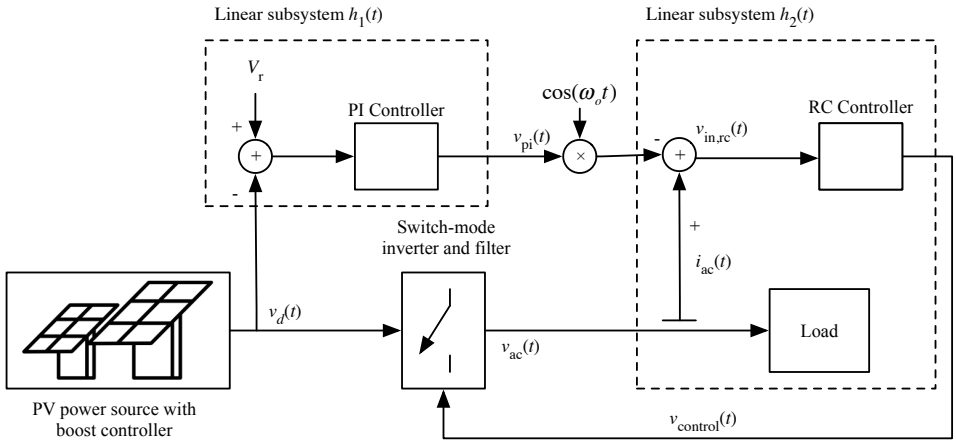

Figure 6.1: High level model of the microgrid investigated in this thesis.

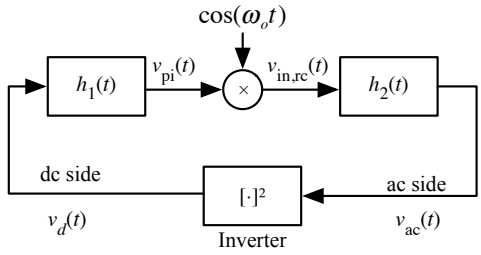

Figure 6.2: Abstraction of the microgrid model.

and the inverter. An abstraction of figure 6.1 where we again use the assumption in (4.1) stating that $v_{\text{ac}}(t) \propto v_{\text{control}}(t)$ is shown in figure 6.2. The linear subsystems $h_1(t)$ and $h_2(t)$ is linear systems, so that the amplitude and phase values may change, but not the frequency value. From appendix C we see that influence from the ac voltage $v_{\text{ac}}(t)$ through the inverter on $v_d(t)$ is given by

$$v_d(t) = V_a \cdot v_{\text{ac}}^2(t) + V_d \tag{6.1}$$

where V_a is a constant. Note that this influence from the ac side on the dc side is opposite of the energy flow. Equation (6.1) states that the oscillatory part of the dc voltage $v_d(t)$ discussed in section 3.3 is generally given by

$$\tilde{v}_d(t) \propto v_{\text{ac}}^2(t) \tag{6.2}$$

The feedback effect form the dc bus $v_d(t)$ to the ac voltage $v_{\text{ac}}(t)$ through the controller is given by

$$v_{\text{ac}}(t) = \big((v_d(t) * h_1(t)) \cdot \cos(\omega_o t)\big) * h_2(t) \tag{6.3}$$

Let us assume a pure sinewave with frequency ω_o on the ac voltage $v_{\text{ac}}(t)$. We will now demonstrate how ideal conditions will result in odd harmonics on the output voltage, even if the load is linear. We mark the initial variables with subscript 0. We will start with

$$v_{\text{ac},0}(t) = V_{\text{ac},0} \cos(\omega_o t) \tag{6.4}$$

this results in a feedback to the dc voltage

$$\begin{aligned} v_{d,0}(t) &= \frac{V_a V_{\text{ac}}^2}{2} \cos(2\omega_o t) + \big(\frac{V_a V_{\text{ac}}^2}{2} + V_d\big) \\ &= V_{a,0} \cos(2\omega_o t) + V_{d,0} \end{aligned} \tag{6.5}$$

As discussed in the previous chapters, a $2\omega_o$ harmonic on the dc voltage $v_{d,0}(t)$ will give a feedback to the ac side as given by

$$\begin{aligned} v_{\text{ac},1}(t) &= \big((v_{d,0}(t) * h_1(t)) \cdot \cos(\omega_o t)\big) * h_2(t) \\ &= \big((\tilde{V}_d \cos(2\omega_o t) * h_1(t)) \cdot \cos(\omega_o t)\big) * h_2(t) \\ &= V_{\text{ac,a1}} \cos(\omega_o t - \phi_{\text{ac,a1}}) + V_{\text{ac,b1}} \cos(3\omega_o t - \phi_{\text{ac,b1}}) \end{aligned} \tag{6.6}$$

1 is added in subscript to mark the completion of the first full feedback loop iteration. This positive feedback loop is the same effect as our initial hypothsis from section 3.3. On the ac side voltage $v_{\text{ac},1}(t)$ we have two odd harmonics and one even on the dc side $v_{d,0}(t)$.

We will now generalize this hypothesis. First, we postulate that on the ac side, we will have all odd harmonics of ω_o, and all even harmonics of ω_o on the dc side. Appendix D shows that if the ac voltage $v_{\text{ac}}(t)$ only contain odd harmonics, then the dc voltage will be written by

$$v_d(t) = V_d + \sum_{i=1}^{\infty} \tilde{V}_{d,i} \cos(2i \cdot \omega_o t - \phi_{d,i}). \tag{6.7}$$

This means that if we only have odd harmonics on the ac $v_{\text{ac}}(t)$, we will get even harmonics on the dc $v_d(t)$. In general, if a sum of even harmonics is multiplied with its fundamental harmonics we get that

$$\begin{aligned} \cos(\omega_o t) \cdot \sum_{i=1}^{\infty} V_i' \cdot \cos(2i \cdot \omega_o t) &= \sum_{i=1}^{\infty} \frac{V_i'}{2} \cdot \cos\big((2i+1)\omega_o t\big) \\ &\quad + \sum_{i=1}^{\infty} \frac{V_i'}{2} \cdot \cos\big((2i-1)\omega_o t\big) \\ &= \sum_{i=1}^{\infty} V_i \cdot \cos\big((2i+1)\omega_o t\big). \end{aligned} \tag{6.8}$$

This means that the feedback from the dc bus $v_d(t)$ through the controller to the ac side should result in an ac voltage

$$\begin{aligned} v_{\text{ac}}(t) &= \big((v_d(t) * h_1(t)) \cdot \cos(\omega_o t)\big) * h_2(t) \\ &= \Big(\Big(\sum_{i=1}^{\infty} \tilde{V}_{d,i} \cos(2i \cdot \omega_o t - \phi_{d,i})\Big) * h_1(t)\Big) \cdot \cos(\omega_o t)\big) * h_2(t) \\ &= \sum_{i=1}^{\infty} V_{\text{ac,i}} \cdot \cos\big((2i+1)\omega_o t - \phi_{\text{ac,i}}\big). \end{aligned} \tag{6.9}$$

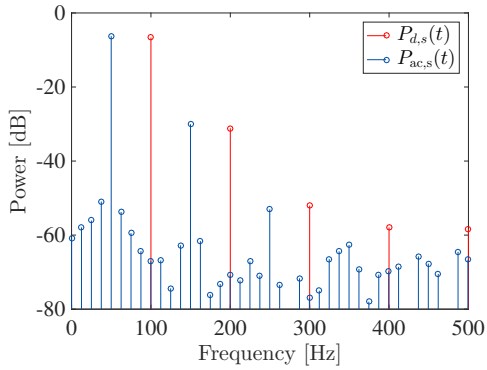

Figure 6.3: Power spectrum of simulated dc bus $v_{d,\mathrm{s}}(t)$ and ac voltage $v_{\mathrm{ac,s}}(t)$. The spectrum is calculated using (3.1) where $N = 20$ K and $F_s = 1$ MHz.

Equation (6.7) and (6.9) shows that odd harmonics on the ac voltage $v_{\mathrm{ac}}(t)$ causes even harmonics on the dc bus $v_d(t)$, and that even harmonics on $v_d(t)$ cause more odd harmonics on $v_{\mathrm{ac}}(t)$. The generalized hypothesis is analytically sound because we initialize with one odd harmonic ω_o on $v_{\mathrm{ac}}(t)$. The power spectra of the simulated ac voltage $v_{\mathrm{ac,s}}(t)$ and the dc voltage $v_{d,\mathrm{s}}(t)$ using the Simulink simulation in section 5 is shown in figure 6.3. The power spectrum of the dc bus $v_{d,s}(t)$ only contains even harmonics. The ac side mainly contains odd harmonics. The even harmonics can be explained by the vertical asymmetry of pulse-width modulation.

6.1 Discussion

Since the analytical and simulated investigation showed a dominance of odd harmonics on the ac side, and even harmonics on the dc side, we conclude with a general hypothesis that a feedback loop mainly causes the distortions seen on v in chapter 4. The feedback loop originates on the ac side and cascades through the inverter to the dc side, and back to the ac side via the control unit. The degree of the distortions will vary depending on the tuning and setup of the controller.

Chapter 7

Reflections on the hypothesis

In the previous chapters, we have presented and tested a hypothesis, and then generalized it analytically. The generalized hypothesis was validated with a simulation. The first proposal to the origin of the distortion in the microgrid is in section 3.3 and the generalization is in section 6. In this chapter, we will compare the results from the different approaches to giving a better overview, and summarize the discussions of previous chapters.

The criterion for falsification stated on page 18 in the initial hypothesis were that there must be 10 ms cycles on the instantaneous frequency. Figure 7.1 shows the instantaneous frequency for all approaches. Visual inspection indicates that all procedures have a 10 ms fundamental period variation of its frequency. These res-

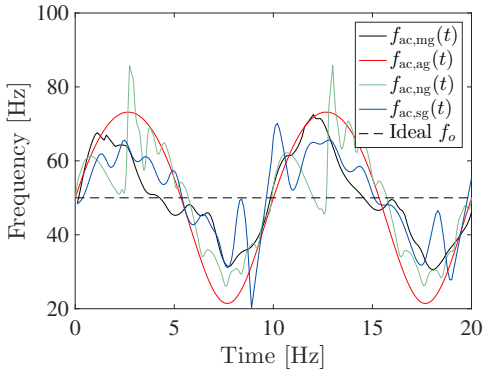

Figure 7.1: The instantaneous frequency from the grid component of the measured waveform $f_{\mathrm{ac,mg}}(t)$, result of the analytic investigation $f_{\mathrm{ac,ag}}(t)$ and its numeric version corrected for pwm $f_{\mathrm{ac,ng}}(t)$, and from the simulation $f_{\mathrm{ac,sg}}(t)$ shown together.

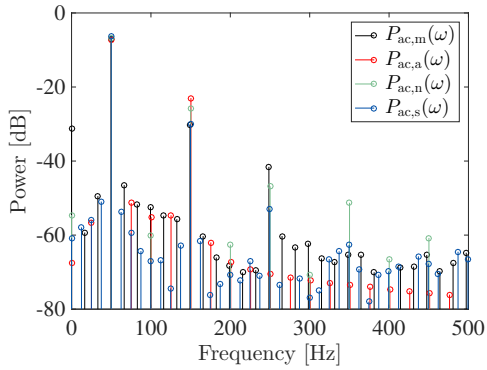

Figure 7.2: The power spectra from the grid component of the measured waveform $P_{\mathrm{ac,m}}(\omega)$, result of the analytic investigation $P_{\mathrm{ac,a}}(\omega)$ and its numeric version corrected for pwm $P_{\mathrm{ac,n}}(t)$, and from the simulation $P_{\mathrm{ac,s}}(\omega)$ shown together.

ults lead us to the conclusion that the hypothesis stated in section 3.3 is a possible explanation of the cause of the distortion. The author does not, however, have any explanation of the somewhat unpredictable variations of the instantaneous frequencies[1]. The instantaneous amplitudes of $v_{\mathrm{ac,mg}}(t)$, $v_{\mathrm{ac,ag}}(t)$, $v_{\mathrm{ac,ng}}(t)$, and $v_{\mathrm{ac,sg}}(t)$ has not been discussed previously and are commented in appendix E.

Both the initial and the generalized hypothesis state that odd harmonics should dominate the power spectrum of the ac voltage $v_{\mathrm{ac}}(t)$. Figure 7.2 shows the power spectra of $v_{\mathrm{ac,x}}(t)$ for the four different approaches discussed in this thesis, where x in subscript indicates the method used. All power spectra are dominated by the fundamental frequency and odd harmonics. Even harmonics are also present and is mainly explained by the vertically asymmetric behavior of $v_{\mathrm{pwm}}(t)$.

The main difference between the hypotheses is the origin of the distortions. The initial hypothesis from section 3.3 attributes the distortions to a single 100 Hz oscillation on the dc voltage $v_d(t)$, amplified by the controller to the ac voltage $v_{\mathrm{ac}}(t)$ that was simultaneously affected by the pulse-width modulation of the inverter. The general hypothesis presented in section 6 states that the origin comes from the ac voltage $v_{\mathrm{ac}}(t)$, resulting in a positive feedback loop that cascades the harmonics. The initial hypothesis was also found to be a particular case of the general one.

Due to these findings, the author argues that the probable cause of the distortions found on the investigated microgrid is a cascading feedback via the microgrid's

[1]Reasons of the variable changes in the instantaneous frequency is of particular interest to the author, and we think it would be interesting to study further using a higher dimension analysis tool such as the Holo Hilbert Spectrum [27]. Unfortunately, this thesis has a limited scope and time.

controller. The Hilbert-Huang transform has been particularly helpful for the author when detecting this distortion, as it showed the 100 Hz oscillation on the instantaneous frequency, leading us to investigate the dc bus and the controller.

Chapter 8

Concluding remarks

This thesis outlines an analysis methodology to investigate the origin of distortions on the voltage waveform $v_{\mathrm{ac}}(t)$ delivered from an isolated microgrid to a load. The method was developed to investigate atypical distortions on ac voltage waveforms on a microgrid at the Royal University of Bhutan's College of Science and Technology. The method uses the traditional Periodogram, and the Hilbert-Huang transform, which, as known to the author, has not been used previously to examine electrical power systems. The Hilbert spectrum of the ac voltage $v_{\mathrm{ac}}(t)$ showed a 10 ms oscillatory behavior on its instantaneous grid frequency. Distortions on the ac voltage are usually attributed to nonlinear loads, but this could not explain the distortions observed, as the load on the actual microgrid was mostly linear. From this, we hypothesized that the distortions could be attributed to the propagation of the inherent 100 Hz oscillatory power that characterizes single phase electrical systems. The hypothesis was tested by analytically examining how the intrinsic oscillatory component of the dc voltage $v_d(t)$ propagates through the controller feedback of the PV inverter system; resulting in an amplitude modulation, according to the analysis of the mathematical expression of the output voltage waveform of the inverter. By assuming that the 100 Hz oscillation caused the distortion, we managed to explain the distortions using the methodology on the voltage waveforms from the analytical model. A Simulink model to simulate the system was used to validate the findings.

The initial hypothesis was then expanded to a general harmonic analysis of a positive feedback loop cascading from the ac side and through the inverter to the dc side and then back to the ac side via the controller. The power spectra of the measured ac voltage $v_{\mathrm{ac,m}}(t)$, the analytically calculated $v_{\mathrm{ac,a}}(t)$, the numerically estimated ac voltage $v_{\mathrm{ac,n}}(t)$, and the simulated voltage $v_{\mathrm{ac,s}}(t)$ were all dominated by odd

harmonics. The odd harmonics on $v_{\mathrm{ac,s}}(t)$ is a necessity for the generalized hypothesis, although it could also be explained by non-ideal low pass filtering of the pulse-width modulation's effect on the ac voltage $v_{\mathrm{ac,s}}(t)$. A simulation of the dc bus voltage $v_{d,s}(t)$ was therefore used. Its power spectrum showed a clear dominance of even harmonics, further strengthening our general hypothesis about the positive feedback loop. This thesis, therefore, argues that the primary cause of the distortions found on the microgrid in Bhutan can be attributed to the positive feedback loop cascading and creating odd harmonics on the ac voltage.

Bibliography

[1] United Nations Sustainability Goals, "Affordable clean energy: why it matters." http://www.un.org/sustainabledevelopment/wp-content/uploads/2016/08/7_Why-it-Matters_Goal-7_CleanEnergy_2p.pdf. [Online; accessed 24-October-2016].

[2] International Energy Agency, "About energy access." https://www.iea.org/topics/energypoverty/. [Online; accessed 30-June-2016].

[3] H. Duus, S. Mandelli, M. Molinas, and O. B. Fosso, "A methodology for supporting the planning of microgrids based on composable tools: A case in bhutan," in *Energy (IYCE), 2015 5th International Youth Conference on*, pp. 1–6, May 2015.

[4] H. Duus, *An Integrated Tool for Microgrid Design in Rural Areas*. Trondheim, Norway: Norwegian University of Science and Technology, 2015.

[5] G. Hillestad, *Design av et utviklingsverktøy for microgrids - En fleksibel og effektiv tilnærming*. Trondheim, Norway: Norwegian University of Science and Technology, 2016.

[6] G. Kulia, M. Molinas, L. Lundheim, and B. rn B. Larsen, "Towards a real-time measurement platform for microgrids in isolated communities.," *Procedia Engineering*, vol. 159C, pp. 94–103, 2016.

[7] N. E. Huang, Z. Shen, S. R. Long, M. C. Wu, H. H. Shih, Q. Zheng, N.-C. Yen, C. C. Tung, and H. H. Liu, "The empirical mode decomposition and the Hilbert spectrum for nonlinear and non-stationary time series analysis," *Proceedings: Mathematical, Physical and Engineering Sciences*, vol. 454, no. 1971, pp. 903–995, 1998.

[8] G. Kulia, M. Molinas, and L. Lundheim, "Tool for detecting waveform distortions in inverter-based microgrids: a validation study," in *2016 IEEE Global Humanitarian Technology Conference (GHTC 2016)*, (Seattle, USA), Oct. 2016.

[9] P. C. Sen, *Principles of Electric Machines and Power Electronics*. New York: Wiley, 3 ed., 2013.

[10] J. G. Proakis and D. G. Manolakis, *Digital Signal PRocessing: Principles, Algorithms, and Applications*. New Jersey: Pearson, 4 ed., 2013.

[11] B. Boashash, "Estimating and interpreting the instantaneous frequency of a signal - part 1: Fundamentals," *Proceedings of the IEEE*, vol. 80, no. 4, pp. 520–538, 1992.

[12] Z. Wu and N. E. Huang, "A study of the characteristics of white noise using the empirical mode decomposition method," *Proceedings of the Royal Society of London A: Mathematical, Physical and Engineering Sciences*, vol. 460, no. 2046, pp. 1597–1611, 2004.

[13] Z. Wu, "HHT Matlab program." http://rcada.ncu.edu.tw/research1_clip_program.htm. [Online; accessed 16-September-2016].

[14] S. L. Hahn, "On the uniqueness of the definition of the amplitude and phase of the analytic signal," *Signal Processing*, vol. 83, no. 8, pp. 1815 – 1820, 2003.

[15] B. Boashash, *Time-Frequency Signal Analysis and Processing*. UK: Elsevier, 2 ed., 2003.

[16] E. Bedrosian, "A product theorem for Hilbert transforms," *United States Air Force Project Rand*.

[17] N. E. Huang, Z. Wu, S. R. Long, K. C. Arnold, X. Chen, and K. Blank, "On instantaneous frequency," *Advances in Adaptive Data Analysis*, vol. 01, no. 02, pp. 177–229, 2009.

[18] F. N. Fritsch and R. E. Carlson, "Monotone piecewise cubic interpolation," vol. 17, pp. pp. 238–246, 1980.

[19] W. H. Press, B. P. Flannery, S. A. Teukolsky, and W. T. Vetterling, *Numerical Recipes in Fortran 77: The Art of Scientific Computing*. Cambridge, UK: Cambridge University Press, 2 ed., 1992.

[20] B. Boashash, "Estimating and interpreting the instantaneous frequency of a signal - part 2: Algorithms and applications," *Proceedings of the IEEE*, vol. 80, no. 4, pp. 540–568, 1992.

[21] N. Mohan, T. M. Undeland, and W. P. Robbins, *Power electronics - Converters, Applications, and Design*. New York: Wiley, 3 ed., 2003.

[22] K. Popper, *The Logic of Scientific Discovery*. New York: Basic Books, 1959.

[23] T. Gilovich, D. Griffin, and D. Kahneman, *Heuristics and Biases: The psychology of intuitive judgment*. Cambridge, UK: Cambridge University Press, 1 ed., 2002.

[24] R. Teodorescu, M. Liserre, and P. Rodriguez, *Grid Converters for Photovoltaic and Wind Power Systems*. Sussex, UK: Wiley, 2011.

[25] Y. Yang, F. Blaabjerg, and H. Wang, "Constant power generation of photovoltaic systems considering the distributed grid capacity," in *2014 IEEE Applied Power Electronics Conference and Exposition - APEC 2014*, pp. 379–385, March 2014.

[26] E. Kreyszig, *Advanced Engineering Mathematics*. New York: Wiley, 9 ed., 2006.

[27] N. E. Huang, K. Hu, A. C. C. Yang, H.-C. Chang, D. Jia, W.-K. Liang, J. R. Yeh, C.-L. Kao, C.-H. Juan, C. K. Peng, J. H. Meijer, Y.-H. Wang, S. R. Long, and Z. Wu, "On Holo-Hilbert spectral analysis: a full informational spectral representation for nonlinear and non-stationary data," *Philosophical Transactions of the Royal Society of London A: Mathematical, Physical and Engineering Sciences*, vol. 374, no. 2065, 2016.

[28] K. Rottmann, *Matematisk Formelsamling (Matematische Formelsammlung)*. Oslo, Norway: Spektrum forlag, 2006.

Appendix A

Example of the Hilbert transform and Normalized Quadrature Method

Lets consider two voltage waveforms $v_1(t)$ and $v_2(t)$. They are given by

$$v_1(t) = \cos(2\pi 50t) \tag{A.1}$$

and

$$v_2(t) = \cos(2\pi 50t) \cdot \big(1 + 7u(t-\tau)\big) \tag{A.2}$$

where $u(t-\tau)$ is a *step function*.

A.1 Hilbert transform

By using the Bedrosian theorem in section 3.2.1 we know that the amplitude $\check{V}_1 = 1$ and phase $\check{\theta}_1(t) = 2\pi 50t$ of $v_1(t)$ is well defined using the Hilbert transform because their power spectra are disjoint. The analytic signal was numerically calculated using discrete Hilbert transform in Matlab. By using the definition of instantaneous frequency in (3.15) and the phase $\check{\theta}_1(t) = 2\pi 50t$ we calculated the instantaneous frequency $f_1(t)$ of $v_1(t)$. Both $v_1(t)$ and $f_1(t)$ are shown in figure A.1. We can see that the frequency $f_1(t)$ is constant 50 Hz, as expected from (A.1). For $v_2(t)$ we want to estimate

$$V_2(t) = 1 + 7u(t-\tau) \tag{A.3}$$

and

$$\theta_2(t) = 2\pi 50t. \tag{A.4}$$

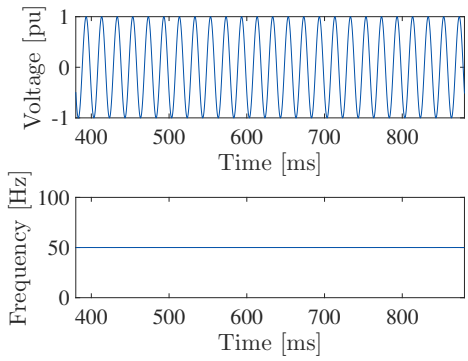

Figure A.1: Voltage waveform $v_1(t)$ and its instantaneous frequency $f_1(t)$ calculated using discrete Hilbert transform. The Bedrosian theorem is satisfied for $v_1(t)$.

The power spectrum of $V_2(t)$ and $\cos(\theta_1)$ is shown in figure A.2. The Bedrosian theorem is not satisfied for $v_2(t)$ because the the power spectra overlap as shown in figure A.2. The voltage waveform $v_2(t)$ and its instantaneous frequency $f_2(t)$ is shown in figure A.3(a). The step function is affecting the frequency f_2 before the step, giving it considerable fluctuations. This means that the Hilbert transform does not calculate the instantaneous frequency correctly for $v_2(t)$.

A.2 Normalized Quadrature method

The limitation stated by the Bedrosian theorem that is shown above is not apparent in the normalized quadrature method (NQM). By using NQM to estimate the amplitude $V_2(t)$ and phase $\theta_2(t)$ of $v_2(t)$ we get the results shown in figure A.3(b). The instantaneous frequency $f_2(t)$ is now constant before and after the transition.

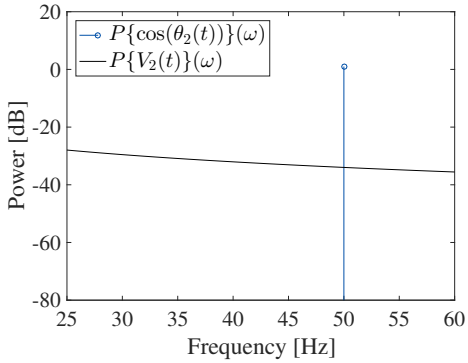

Figure A.2: Power spectra of $V_2(t)$ and $\cos\big(\theta_2(t)\big)$.

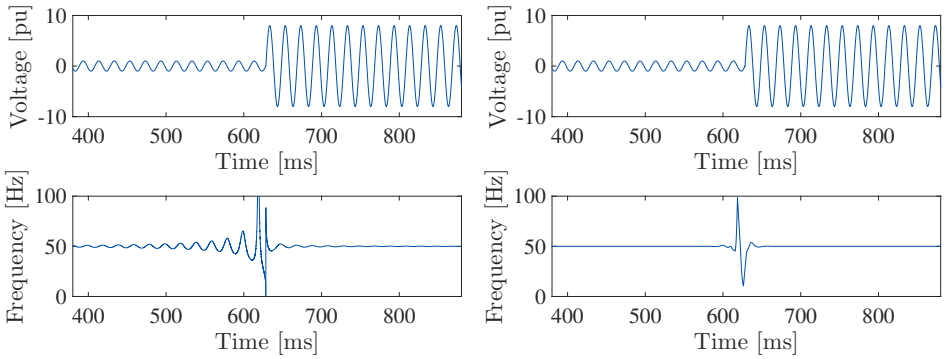

(a) Voltage waveform $v_2(t)$ and its instantaneous frequency $f_2(t)$ calculated using discrete Hilbert transform. The Bedrosian theorem is not satisfied for v_2.

(b) Voltage waveform $v_2(t)$ and its instantaneous frequency $f_2(t)$ calculated using the normalized quadrature method.

Figure A.3: Voltage waveform $v_2(t)$ and its instantaneous frequency $f_2(t)$ calculated using the discrete Hilbert transform and normalized quadrature method.

Appendix B

Calculation of $v_{\text{control}}(t)$

From (3.31) we have that $v_d(t) = V_d + \tilde{V}_d \cos(2\omega_o t)$. We can set this into (B.1), and by assuming $v_r = V_d$, we get that

$$v_e(t) = \tilde{V}_d \cos(2\omega_o t) \tag{B.1}$$

Equation (4.4) gives us that $v_{\text{pi}}(t)$ is given by

$$v_{\text{pi}}(t) = \tilde{V}_d\big(K_p \cdot \cos(2\omega_o t) + \frac{K_i}{2\omega_o}\sin(2\omega_o t)\big) \tag{B.2}$$

Leading to an input to the RC on the form

$$v_{\text{in,rc}} = R_k \cdot i_{\text{ac}} + \cos(\omega_o t)\big(B_1 \cos(2\omega_o t) + B_2 \sin(2\omega_o t)\big) \tag{B.3}$$

where $B_1 = K_p \cdot \tilde{V}_d$, and $B_2 = \frac{K_i}{2\omega_o}\tilde{V}_d$. R_k is a constant. As

$$\cos(2\omega_o t) \cdot \cos(\omega_o t) = \frac{1}{2}\big(\cos(\omega_o t) + \cos(3\omega_o t)\big) \tag{B.4}$$

and

$$\sin(2\omega_o t) \cdot \cos(\omega_o t) = \frac{1}{2}\big(\sin(\omega_o t) + \sin(3\omega_o t)\big) \tag{B.5}$$

the resulting $v_{\text{control}}(t)$ from the Resonant Controller will be

$$\begin{aligned} v_{\text{control}}(t) = {} & C_p \cdot v_{\text{in,rc}}(t) \\ & + C_i\big(\frac{B_1}{2}\cos(\omega_o t) + \frac{B_2}{2}\sin(\omega_o t)\big) \\ & + v_{\text{ac,rc}}(t) \end{aligned} \tag{B.6}$$

where $v_{\text{ac,rc}}(t) = A \cdot \big(C_i i_{\text{ac}}(t) * h_{\text{rc}}(t) + C_p i_{\text{ac}}\big)$ and $h_{\text{rc}}(t)$ is the impulse response to a band-pass filter with center frequency ω_o.

Equation (B.6) can be rewritten on the form

$$\begin{aligned} v_{\text{control}}(t) = {} & V_{\text{g1}} \cos(\omega_o t) + V_{\text{g2}} \sin(\omega_o t) \\ & + V_{\text{am1}} \cos(2\omega_o t) \cos(\omega_o t) \\ & + V_{\text{am2}} \sin(2\omega_o t) \cos(\omega_o t) \\ & + v_{\text{feedback}}(t) \end{aligned} \tag{B.7}$$

where $V_{\text{g1}} = C_i \frac{B_1}{2}$, $V_{\text{g2}} = C_i \frac{B_2}{2}$, $V_{\text{am1}} = B_1 \cdot C_p$, $V_{\text{am2}} = B_2 \cdot C_p$, and $v_{\text{feedback}}(t) = R_k \cdot C_p i_{\text{ac}}(t) + v_{\text{ac,rc}}(t)$.

By using the trigonometric identity that

$$a \cos(\omega_o t) + b \sin(\omega_o t) = G \cos(\omega_o t - \phi_G) \tag{B.8}$$

where $G = \sqrt{a^2 + b^2}$ and $\phi_G = \arctan\big(\frac{b}{a}\big)$ we get that

$$\begin{aligned} v_{\text{control}}(t) = {} & V_{\text{g}} \cos(\omega_o t - \phi_g) \\ & + V_{\text{am}} \cos(2\omega_o t - \phi_{\text{am}}) \cos(\omega_o t) \\ & + v_{\text{feedback}}(t) \end{aligned} \tag{B.9}$$

with $V_{\text{g}} = \sqrt{V_{\text{g1}}^2 + V_{\text{g2}}^2}$, $V_{\text{am}} = \sqrt{V_{\text{am1}}^2 + V_{\text{am2}}^2}$,
$\phi_g = \arctan\Big(\frac{V_{\text{g2}}}{V_{\text{g1}}}\Big)$, and $\phi_{\text{am}} = \arctan\Big(\frac{V_{\text{am2}}}{V_{\text{am1}}}\Big)$.

We assume $v_{\text{feedback}} \approx 0$. This gives us that

$$\begin{aligned} v_{\text{control}}(t) = {} & \frac{C_i}{2} \cdot \tilde{V}_d \sqrt{K_p^2 + \big(\frac{K_i}{2\omega_o}\big)^2} \cos\left(\omega_o t - \arctan \frac{K_i}{2\omega_o K_p}\right) \\ & + C_p \cdot \tilde{V}_d \sqrt{K_p^2 + \big(\frac{K_i}{2\omega_o}\big)^2} \cos\left(2\omega_o t - \arctan \frac{k_i}{2\omega_o K_p}\right) \cos(\omega_o t) \end{aligned} \tag{B.10}$$

This can be rewritten on the form

$$\begin{aligned} v_{\text{control}}(t) = {} & \big(\frac{C_i}{2} + C_p\big) \cdot \tilde{V}_d \sqrt{K_p^2 + \big(\frac{K_i}{2\omega_o}\big)^2} \cos\left(\omega_o t - \arctan \frac{K_i}{2\omega_o K_p}\right) \\ & + C_p \cdot \tilde{V}_d \sqrt{K_p^2 + \big(\frac{K_i}{2\omega_o}\big)^2} \cos\left(3\omega_o t - \arctan \frac{k_i}{2\omega_o K_p}\right) \end{aligned} \tag{B.11}$$

we define

$$1 \text{ pu} = \tilde{V}_d \sqrt{K_p^2 + \left(\frac{K_i}{2\omega_o}\right)^2} \tag{B.12}$$

By using the tuning from table 4.1 we get that

$$\begin{aligned} v_{\text{control}}(t) = \frac{3}{2} \text{ pu} \cdot \cos\left(2\pi 50 t - \arctan\frac{1}{100\pi}\right) \\ + 1 \text{ pu} \cdot \cos\left(2\pi 50 t - \arctan\frac{1}{100\pi}\right) \end{aligned} \tag{B.13}$$

To relate this to expression (4.8) we get that

$$C_1' = \frac{3}{2} \text{ pu}, \tag{B.14}$$

$$C_2' = 1 \text{ pu}, \tag{B.15}$$

$$\phi_1' = \phi_2' = \arctan\frac{1}{100\pi} \approx 1.01321 \text{ mrad}, \tag{B.16}$$

and

$$B' \approx 0 \tag{B.17}$$

Appendix C

The ac voltage's effect on the dc bus through the inverter

This appendix shows how to get a general expression of the ac voltage $v_{\text{ac}}(t)$'s impact on the dc bus $v_d(t)$. We assume no energy loss in any filters or the inverter. By also assuming a linear load we get that the ac power is given by

$$P_{\text{ac}}(t) = \frac{v_{\text{ac}}^2(t)}{R_{\text{load}}} \tag{C.1}$$

and on the dc side we have that

$$P_d(t) = v_d(t) \cdot i_d(t). \tag{C.2}$$

We also know that the dc current can be written as

$$i_d(t) = \frac{v_d(t) - V_s}{R_s} \tag{C.3}$$

where V_s is the supply voltage and R_s is the line impedance as shown in figure 3.9. By assuming $V_d \gg \tilde{v}_d(t)$ and $V_s \approx V_d$ we get that

$$P_d(t) = \frac{V_d \cdot v_d(t) + V_d^2}{R_s} \tag{C.4}$$

We assume the ac power is assumed equal to the dc power so that

$$P_d(t) = P_{\text{ac}}(t) \tag{C.5}$$

this gives us that

$$\frac{V_d \cdot v_d(t) - V_d^2}{R_s} = \frac{v_{\text{ac}}^2(t)}{R_{\text{load}}} \tag{C.6}$$

This means that we can write the dc voltage as

$$v_d(t) = \frac{R_s}{R_{\text{load}}} \frac{v_{\text{ac}}^2(t)}{V_d} + V_d \tag{C.7}$$

This can be rewritten as

$$v_d(t) = V_a \cdot v_{\text{ac}}^2(t) + V_d \tag{C.8}$$

where

$$V_a = \frac{R_s}{R_{\text{load}} \cdot V_d} \tag{C.9}$$

Appendix D

Square of sum containing odd harmonics

This appendix will concern the square of a sum of odd harmonics and show how it result in even harmonics. The square of a sum [28] is given by

$$\Big(\sum_{i=1}^{\infty} v_i(t)\Big)^2 = \sum_{i=1}^{\infty} v_i^2(t) + 2\sum_{i=1,k\neq i}^{\infty} v_i(t)\cdot v_k(t) \tag{D.1}$$

We also have that the product of two odd harmonics is given by

$$\begin{aligned}\cos((2i+1)\omega_o t)\cdot\cos((2k+1)\omega_o t) = \frac{1}{2}\cos\big(2(i-k)\omega_o t\big) \\ + \frac{1}{2}\cos\big(2(i+k+2)\omega_o t\big)\end{aligned} \tag{D.2}$$

By assuming $v_i(t)$ to be an odd harmonic on the form

$$v_i(t) = V_i\cos\big((2i+1)\omega_o t\big) \tag{D.3}$$

and putting (D.2) into (D.1) we get that

$$\begin{aligned}\Big(\sum_{i=1}^{\infty}\cos\big((2n+1)\omega_o t\big)\Big)^2 = \frac{1}{2}\sum_{i=1}^{\infty}V_i + \frac{1}{2}\sum_{i=1}^{\infty}V_i\cos\big(4(n+1)\omega_o t\big) \\ + \sum_{i=1,k\neq i}^{\infty}V_iV_k\cos\big(2(i-k)\omega_o t\big) \\ + \sum_{i=1,k\neq i}^{\infty}V_iV_k\cos\big(2(i+k+2)\omega_o t\big).\end{aligned} \tag{D.4}$$

Equation (D.5) covers all even harmonics, so it can be rewritten as

$$\Big(\sum_{i=1}^{\infty}\cos\big((2n+1)\omega_o t\big)\Big)^2 = \frac{1}{2}\sum_{i=1}^{\infty}V_i + \sum_{i=1}^{\infty}V_{e,i}\cos\big(2i\cdot\omega_o t\big) \tag{D.5}$$

Appendix E

Comments on amplitude variations

The instantaneous amplitudes for all approaches previously discussed were estimated using the normalization process. The amplitudes have not been commented further in the previous chapters. Figure E.1 shows the instantaneous amplitudes calculated using the different methods. All amplitudes are close to constant and right below one pu. The amplitude of the grid IMF of the measured voltage $v_{\mathrm{ac,m}}(t)$ had the largest fluctuations, with a variation less than ± 2.5 %. The comparison between the instantaneous frequencies of the grid component of $v_{\mathrm{ac,m}}(t), v_{\mathrm{ac,a}}(t)$, $v_{\mathrm{ac,n}}(t)$ and $v_{\mathrm{ac,s}}(t)$ is more trivial when the amplitudes are close to constant.

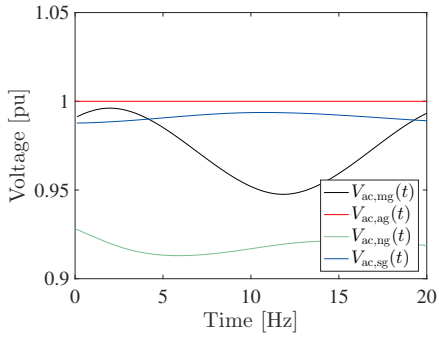

Figure E.1: The instantaneous amplitudes from the grid component of the measured waveform $V_{\mathrm{ac,mg}}(t)$, result of the analytic investigation $V_{\mathrm{ac,ag}}(t)$, and from the simulation $V_{\mathrm{ac,sg}}(t)$ shown together.